Investigating the impact of wellbore lateral heat transfer on the performance of high-temperature aquifer thermal energy storage system by the coupling of wellbore and reservoir simulators

Guoqiang Yan [a], Pål Østebø Andersen [b], Yangyang Qiao [a],*,
Dimitrios Georgios Hatzignatiou [c], Bo Feng [d], Thomas Kohl [a]

[a] Institute of Applied Geosciences, Karlsruhe Institute of Technology, Karlsruhe, 76131, Germany
[b] Department of Energy Resources, University of Stavanger, Stavanger, 4068, Norway
[c] Department of Petroleum Engineering, University of Houston, Houston, TX, 77204, USA
[d] College of New Energy and Environment, Jilin University, Changchun, 130021, China

ARTICLE INFO

ABSTRACT

This study investigates the often-overlooked impact of wellbore lateral heat transfer on high-temperature aquifer thermal energy storage (HT-ATES) systems, focusing on the Swiss Bern project. We coupled our in-house wellbore simulator (Moskito) with the reservoir simulator (PorousFlow) under the MOOSE framework to analyze wellbore heat loss. Utilizing both numerical and analytical approaches, we reveal how wellbore heat loss affects HT-ATES performance compared to previous studies that ignored it. Our sensitivity analysis examines various wellbore configurations and operational parameters, evaluating performance indicators including extracted energy, wellbore lateral heat loss fraction, and reservoir heat loss fraction. Key findings include: a more than 10 % difference between the analytical and numerical calculations of wellbore lateral heat loss. Smaller wellbore diameters, such as 6.75 inches, enhance energy recovery efficiency by enabling larger fluid extraction volumes. Low thermal conductivity wellbore casing materials (e.g., 0.045 W m^{-1}•K^{-1}) could reduce wellbore lateral heat loss by 51.4 %. Although energy recovery efficiency declines with more supporting wells during the initial storage cycle, three supporting wells yield the best performance in later cycles due to larger extracted fluid volumes. High flow rates (e.g., 25 L s^{-1}) enhance energy recovery efficiency by decreasing heat losses through faster fluid movement, which reduces residence time and thermal diffusion. While high fluid injection temperatures (e.g., 210 °C) increase heat losses, overall heat loss fractions decrease due to significant injected energy. This study highlights the critical role of wellbore lateral heat loss in evaluating the performance of the HT-ATES system, providing insights on how to design and optimize these systems.

Nomenclature

A	wellbore cross-sectional area, m^2
C	conversion factor
c_p	specific heat capacity, J·m^{-3}·K^{-1}
d	wellbore diameter, m
E	Energy, J
f	friction factor, -
F	mass or energy flux vector, kg·m^2·s^{-1} or W·m^{-2}
g	gravitational acceleration, m·s^{-2}
h	specific enthalpy, J·kg^{-1}
k	rock permeability, m^2
K	bulk modulus, m

(continued on next column)

(continued)

L	length, m
M	mass or energy density term, kg·m^{-3} or J·m^{-3}
n	time step, -
p	pressure, Pa
q	mass or heat source term, kg·m^{-3} s^{-1} or W·m^{-3}
Q	volumetric flow rate, kg·m^{-3}
r	wellbore radius, m
t	time, s
T	temperature, K
$\boldsymbol{u}$	Darcy velocity, m·s^{-1}
u	velocity, m·s^{-1}

(continued on next page)

* Corresponding author.
  E-mail address: yangyang.qiao@kit.edu (Y. Qiao).

(*continued*)

U	heat transfer coefficient, $\mathrm{W \cdot m^{-1} \cdot K^{-1}}$
V	volume, $\mathrm{m^3}$
WI	well index, $\mathrm{m^3}$
x	x-coordinate, m
y	y-coordinate, m
z	z-coordinate (positive upward), m
Greek symbol	
α	fraction, -
β	convective heat transfer coefficient, -
η	energy recovery efficiency, -
θ	dip angle between the wellbore direction and the vertical direction, ∘
λ	thermal conductivity, $\mathrm{W \cdot m^{-1} \cdot K^{-1}}$
μ	dynamic viscosity, Pa·s
ρ	density, $\mathrm{kg \cdot m^{-3}}$
ϕ	porosity, -
Δ	grid size, m
Subscripts and superscripts	
0	initial
ana	analytical
bh	borehole
cas	casing wall
cem	cement
cf	cement/formation interface
ci	inside casing
co	outside casing
con	convective
cond	conduction
cp	coupling
e	effective
ele	element
ext	extraction
EG	energy
f	formation
fa	far-field
fft	fluid film in tubing and the tubing wall
flow	fluid flow
i	equation type, -
inj	injection
ins	tubing insulation
l	liquid
los	loss
MS	mass
ne	nearest
nhl	no heat loss
num	numerical
r	reservoir
rad	radial
s	solid
ti	inside tubing
to	outside tubing
w	wellbore
xx	length direction
yy	width direction

1. Introduction

The intensive use of fossil energy sources over the past few decades has significantly increased atmospheric carbon dioxide concentrations, contributing to various climate change challenges (EIA, 2009; Ürge-Vorsatz et al., 2015; EU, 2010). To achieve the Paris climate agreement (UN, 2015), many countries are actively adopting strategies that include sustainable energy sources based on their strengths and needs (Jäger-Waldau, 2007; Kim et al., 2010; IEA, 2019; Usman et al., 2020; Muhammed and Tekbiyik-Ersoy, 2020). In these strategies, the effective and rational development, and use of geothermal energy sources are key concerns (Barbier, 2002; Sharmin et al., 2023). As energy supply does not usually align with demand on a seasonal basis, thermal energy storage methods, such as Aquifer Thermal Energy Storage (ATES), Borehole Thermal Energy Storage (BTES) and Fractured Thermal Energy Storage (FTES) that utilize the subsurface pore space and its geothermal energy are gaining attention (Dincer, 2002; Henry et al., 2020; van der Roest et al., 2021). In particular, as aquifers are large-scale energy storage formations, ATES have a significant capacity to provide large amounts of heating and cooling to reduce total energy imbalance. Specifically, ATES operates on a seasonal basis (Kallesøe et al., 2020; Huang et al., 2021). During the heat storage phase, excess heat generated from coal- or gas-fired power plants, solar power plants and cogeneration plants is transferred to cold fluid through heat exchangers. The resulting warm fluid transports the heat to the aquifer where it is stored. During the heat extraction phase, the ATES operates oppositely by reversing the direction of fluid flow between the injection and production wells. The stored heat is then recovered from the warm fluid through a heat exchanger and it is used for heating. At the same time, the resulting cold fluid is reinjected into the aquifer (Dickinson et al., 2009).

System performance is the most significant concern for an ATES system (Tsang, 1978; Lee and Lee, 2013; Bloemendal and Hartog, 2018). Previous research on the performance in ATES systems has been analyzing standalone reservoir models under various conditions, including the wellbore design and operation parameters, etc. (Doughty et al., 1982; Kangas and Lund, 1994; Paksoy et al., 2004; Schüppler et al., 2019; Stemmle et al., 2021; Duijff et al., 2023). Among them, Doughty et al. (1982) first introduced a dimensionless factor — energy recovery efficiency — to quantify the thermal performance of a 2D ATES reservoir, defined as the ratio of extracted energy to the injected energy. Using numerical simulation, Sheldon et al. (2021) found that the aquifer thickness and permeability, injection fluid temperature as well as thermal dispersion length dominate the energy recovery efficiency in a single-well 2D ATES system. Sommer et al. (2013) demonstrated that short preferential pathways, short-circuiting and well interference in a heterogeneous 3D doublet ATES system result in the non-full utilization of the aquifer storage capacity and can cause 6 %~15 % lower energy recovery efficiency compared to the homogeneous case, which highlighted the importance of aquifer heterogeneity in the design and optimization of ATES system. Beernink et al. (2024) examined the impact of heat conduction, heat dispersion and buoyancy-driven convection on the energy loss of the stored heat to the aquifer in a 2D ATES system. Their study considered a broad spectrum of realistic operational storage conditions, including injection fluid temperature and flow rate as well as various hydrogeological factors such as aquifer thickness, hydraulic conductivity and anisotropy. Vidal et al. (2022) proposed a dimensional analysis and 3D finite element reservoir numerical model of the ground surface uplift, heat transport and energy efficiency for the Swiss Bern project (high-temperature ATES (HT-ATES)) with wellbore pattern and investigated the energy recovery efficiency and system safety risk. To avoid the negative effect of buoyancy-driven convection on the energy recovery efficiency of the ATES system, van Lopik et al. (2022) conducted a numerical study to examine how multiple partially penetrated wells (i.e., only wellbore screen section, not overall wellbore) can improve the energy recovery efficiency, under different conditions of wellbore operation and reservoir conditions. Brown and Falcone, 2024 built a simplified 3D ATES reservoir model with only one production well and reservoir to investigate the effects of related factors on the wellbore lateral heat transfer to/from the formation and energy recovery efficiency of the ATES system. In this study, we specifically refer to 'lateral heat transfer' as heat transfer occurring between the wellbore and the surrounding formation in the radial direction (i.e., perpendicular to the wellbore axis) only for the non-open-hole section. The term "lateral" was chosen to distinguish this process from axial heat transfer along the wellbore, which also occurs due to fluid movement. A small initial geothermal gradient, low reservoir temperature and high thermal conductivity significantly enhance heat transfer from the wellbore to the surrounding formation. However, the production well was entirely modeled as porous media with a fixed flow rate within the reservoir. The injection wellbore and cooling effect in the reservoir caused by cold fluid re-injection were ignored.

Overall, these works mainly focused on the performance of the ATES system without a detailed study of the 'realistic' wellbore dynamics. The wellbore sections were either simplified as highly permeable porous media or line/point source/sink in the reservoir model. While their

approaches greatly simplify the numerical model and speed up the simulation process, the dynamic fluid flow and heat transfer processes within the wellbore part and more importantly the heat transfer between the wellbore and formation are either overlooked or not sufficiently emphasized to quantitatively evaluate the impact of wellbore lateral heat transfer on system performance. Wellbore lateral heat transfer occurs when the fluid temperature in the wellbore differs from that of the surrounding geological formations. The frequent cycling and temperature changes inherent in ATES systems can amplify wellbore lateral heat transfer compared to more stable geothermal systems with more constant thermal conditions. This can lead to significant energy loss during storage and extraction, impacting system performance. Therefore, it is crucial to quantitatively assess wellbore lateral heat transfer to accurately evaluate and optimize ATES systems, requiring a full coupling model between the wellbore and reservoir.

With analytical, semi-analytical or numerical approaches, many researchers have devoted efforts to investigate the dynamic fluid flow and heat transfer (including the wellbore lateral heat transfer) based on the complete wellbore-reservoir system for the general geothermal development, CO_2 storage, non-typical (i.e., using air or CO_2 as working fluid) energy storage in aquifer (Ramey Jr, 1962; Satter, 1965; Pan and Oldenburg, 2014). Ramey Jr (1962) first presented an analytical approach to quantify the temperature distribution around a 1D injection well by assuming steady fluid flow in the wellbore and steady heat transfer in the 2D surrounding formation. Built on Ramey's work, the wellbore lateral heat transfer was further developed (Satter, 1965; Willhite, 1967; Horne and Shinohara, 1979; Wu and Pruess, 1990) for different injection and production conditions. Specifically, to release the assumptions used in Ramey's solution, Wu and Pruess (1990) provided an analytical approach in a 1D wellbore model for heat exchange between the wellbore and the uniform/layered 2D formation, using the dimensionless time and depth on transient lateral heat transfer coefficient. Hasan and Kabir (1991) developed a 1D wellbore lateral heat transfer model at the formation-wellbore interface using Fourier's law and proposed a new time function to predict the 'transient' temperature distribution in the system. Cheng et al. (2011) presented a new analytical model for transient lateral heat conduction in the 1D steam injection wells, incorporating the wellbore's heat capacity to improve the temperature and heat transfer predictions in the wellbore and surrounding formation. As for the semi-analytical approach, Zhang et al. (2011) proposed a time-convolution approach where only the wellbore (i.e., not formation) is fully discretized and semi-analytical solutions of wellbore lateral heat transfer by neglecting vertical conductive heat flow within the formation and thermal resistance between the cased wellbore and the formation. This approach has been implemented and validated in a highly transient and strongly non-isothermal multi-phase wellbore-reservoir system (Pan and Oldenburg, 2014; Ezekiel et al., 2020). Regarding the numerical study, Xiong et al. (2016) developed a 1D thermal wellbore simulator using a finite difference approach and calculated the heat transfer and temperature variation in the steam-assisted gravity drainage system. They employed the overall heat transfer coefficient from Willhite (1967) and temperature at the cement-formation interface from a 2D formation heat transfer equation including Ramey Jr (1962) approximation approach. Livescu et al. (2008, 2010) developed a series of fully coupled multiphase wellbore-reservoir simulators using the finite volume method. They used the constant overall heat transfer coefficients and transient temperature profiles of the wellbore and reservoir to calculate the wellbore lateral heat transfer based on the formula proposed by Ramey Jr (1962) but the heat conduction term in the open-hole section was not considered between the reservoir and wellbore. Pan and Oldenburg (2014) developed an integrated simulator T2Well using the finite-difference scheme to solve non-isothermal, multiphase and multi-component fluid flow and heat transfer in the fully coupled 1D wellbore and 3D reservoir system. The T2Well has been widely used to calculate the energy recovery efficiency for compressed air or CO_2 energy storage in aquifers (Li et al., 2023a; Oldenburg and Pan, 2013; Li et al., 2023b; Li et al., 2024) and joint compressed air energy storage and ATES (Guo et al., 2017).

While analytical and semi-analytical solutions provide computational efficiency and good approximations of wellbore fluid flow and heat transfer, they rely on assumptions such as steady-state conditions, uniform thermal properties and negligible vertical heat conduction within the formation (Horne and Shinohara, 1979; Hasan and Kabir, 1991; Cheng et al., 2011; Ezekiel et al., 2020), which cannot fully capture transient heat transfer dynamics, complex wellbore geometries and reservoir heterogeneity. In contrast, numerical solutions offer flexibility to incorporate the dynamic variations of temperature in space and time, especially important for the formation of temperature changes due to alternating circulation flows of warm and cold fluids in wellbores. To address the limitations of analytical and semi-analytical approaches due to their assumptions, You et al. (2016) developed a fully implicit model that couples a 1D wellbore with a 3D surrounding formation using the finite difference method. This model incorporates radial Fourier heat conduction flux to calculate wellbore lateral heat transfer. The above reviews show that the wellbore lateral heat transfer has been considered in several specific topics, including general geothermal development, CO_2 storage and compressed air or CO_2 energy storage in aquifers. However, these approaches have not been applied to typical ATES (i.e., using water as a working fluid for thermal energy storage) and also do not reveal the impacts of related parameters on the wellbore lateral heat transfer.

In this study, our focus is on an HT-ATES system in a shallow reservoir (the Swiss Bern project (Vidal et al., 2022)). The motivation of this work is to reveal the impact of wellbore lateral heat transfer on the HT-ATES performance. We have fully coupled the wellbore fluid flow and heat transfer processes, including lateral heat transfer, simulated by our in-house developed wellbore simulator Moskito (Korzani et al., 2019) together with an existing reservoir simulator PorousFlow (Wilkins et al., 2021) under the MOOSE framework (Permann et al., 2020). The coupled model is then used to compute the wellbore lateral heat transfer along the full well trajectory to the surface for quantitative evaluation of the impact of wellbore lateral heat transfer on the HT-ATES performance, specifically for the Bern project. This is done through varying different key wellbore configurations (wellbore diameter, casing thermal conductivity and number of supporting wells) and operational parameters (injection flow rate and injection temperature at the main well). Such investigations can be helpful to design and optimize the HT-ATES system, regarding the choices of the above parameters. In addition, to achieve a complete assessment of HT-ATES systems, it is crucial to consider a range of performance indicators. While energy recovery efficiency can tell how effectively the system retrieves the stored energy, it is not enough to reflect either the system's operational capacity or energy loss due to the wellbore lateral heat transfer to the formation (*wellbore lateral heat loss*) and heating reservoir (*reservoir heat loss*). Therefore, it can be worth considering the extracted energy, wellbore lateral heat loss (fraction) and reservoir heat loss (fraction) as additional performance indicators together with the energy recovery efficiency which was generally treated as the only indicator to evaluate the HT-ATES system performance. It is important to note that the findings in this study are based on the initial phase (1st five years) of HT-ATES system operation. In practice, HT-ATES systems typically require several cycles (<10 years) to reach steady-state conditions, where cycles become nearly identical. The long-term behavior, including trends over 30+ years, may differ from the initial phase and warrants further investigation.

The paper is organized as follows. In Section 1, we present the methodology for fully coupling our in-house developed wellbore simulator and the reservoir simulator under the MOOSE framework. In Section 2, the developed coupled simulation tool is used to model a specific HT-ATES case with different scenarios including varying the wellbore configurations and operational parameters. The obtained results are discussed in Section 3 for the impact of the wellbore lateral heat transfer

Table 1

The mass, energy and momentum equations solved in the coupled wellbore-reservoir simulator.

Equation and term	1D Wellbore	3D Reservoir
Mass (MS) conservation Energy (EG) conservation	$\frac{\partial M_i}{\partial t} + \nabla \cdot F_i - q_i{}^{cp} = 0$ ($i = MS$ or EG)	$\frac{\partial M_i}{\partial t} + \nabla \cdot F_i + q_i{}^{cp} = 0$ ($i = MS$ or EG)
Mass density: M_{MS}	$\rho_l A$	$\varphi \rho_l$
Mass flux: F_{MS}	$\rho_l A u_l$	$\rho_l \boldsymbol{u}_l$
Energy density: M_{EG}	$\rho_l A \left(c_{p,l} T + \frac{u_l{}^2}{2} \right)$	$[\varphi c_{p,l} \rho_l + (1 - \varphi) c_{p,s} \rho_s] T$
Energy flux: F_{EG}	$\rho_l A u_l c_{p,l} T - \lambda_l \nabla (AT)$ $+ \rho_l A u_l \left(\frac{p}{\rho_l} + \frac{u_l{}^2}{2} + gz \cos \theta \right)$	$\rho_l c_{p,l} \boldsymbol{u}_l T - [\varphi \lambda_l + (1 - \varphi) \lambda_s] \nabla T$
Momentum	$\nabla(pA) = \rho_l A g \cos \theta \pm \frac{f \rho_l A u_l{}^2}{2d}$ $\pm \left[\frac{\partial}{\partial t} (\rho_l A u_l) + \nabla (\rho_l A u_l{}^2) \right]$	$\boldsymbol{u}_l = \frac{k}{\mu_l} (-\nabla p + \rho_l g)$

*M is mass or energy density term; F represents mass or energy flux vector; q is mass or heat source term; A means wellbore cross-sectional area; u is velocity; $\boldsymbol{u}$ represents Darcy velocity; z means z-coordinate (positive upward); f is friction factor; d means wellbore diameter; θ represents the angle between the wellbore direction and the vertical direction.

on the HT-ATES performance. Finally, in Section 4, key findings of the design and operation of the HT-ATES system and recommendations for future research are summarized in the conclusion part.

2. Materials and methods

2.1. Equations and coupling methods in a wellbore-reservoir system

The governing equations (Pan and Oldenburg, 2014; Korzani et al., 2019; Wilkins et al., 2021) for fluid flow and heat transfer-transport in the wellbore and reservoir are presented in Table 1. Note that the conservation law for both mass and energy holds the same format. The differences in equations between the wellbore and the reservoir lie in the definitions of energy flux terms and fluid velocity. For the momentum equation, fluid flow in the reservoir takes Darcy's law and Navier-Stokes type of equation for the wellbore flow where the inertial forces are considered. Furthermore, kinetic energy and gravitational potential energy are included in the wellbore heat equation. In contrast, the heat equation for the reservoir does not account for these terms due to the creeping flow in the porous medium.

Regarding the mass and energy coupling between the reservoir and wellbore, two regions are considered: the open-hole and the non-open-hole sections. In the open-hole section, there is mass transfer and energy transfer due to fluid flow (convection) and heat conduction driven by the local temperature gradient. A Peaceman-type equation (Peaceman, 1983) is employed for calculating the source terms in the mass equations for the open-hole section, which is a function of the pressure difference between the reservoir and the wellbore (see Table 2). To ensure accurate and consistent coupling of physical processes, a conversion factor (C) is used to align the differences in scale and resolution between the 1D wellbore and 3D reservoir systems. In this study,

$$C = \begin{cases} (\Delta z)^{-1}, & wellbore; \\ (V_{ele}^r)^{-1}, & reservoir. \end{cases}$$, where Δz is grid block size [m] in the depth

direction, V refers to volume; r means reservoir, ele represents element. The $f(t)$ is dimensionless time function. When time is greater than one week, it can be calculated by $f(t) = \ln \left(2 \sqrt{\frac{\lambda^f}{\rho^f c_p^f} t} \big/ r_{cf} \right) - 0.29$. The well index ($WI^{flow}$) for fluid flow in the Peaceman-type formula (Peaceman, 1983) accounts for the impact of the reservoir grid size, reservoir permeability and wellbore radius, etc. It reflects the well's ability to inject or produce fluid.

$$WI^{flow} = 2\pi \sqrt{k_{xx} k_{yy}} \Delta z \big/ \ln \left(r_e^{flow} / r_{bh} \right) \tag{1}$$

where k_{xx}, k_{yy}, r_{bh} and r_e^{flow} are respectively reservoir permeability [m^2] in the length direction, reservoir permeability [m^2] in the width direction, wellbore radius [m] and effective wellbore radius for fluid flow [m] which can be calculated by (Peaceman, 1983):

$$r_e^{flow} = 0.28 \frac{\sqrt{\sqrt{k_{xx}/k_{yy}}(\Delta x)^2 + \sqrt{k_{yy}/k_{xx}}(\Delta y)^2}}{(k_{xx}/k_{yy})^{1/4} + (k_{yy}/k_{xx})^{1/4}} \tag{2}$$

where Δx is the length [m] and Δy is the width [m] of a grid block.

Similarly, the well index (WI^{cond}) for heat conduction in the Peaceman-type formula (Shi et al., 2024) accounts for the impact of the reservoir grid size, reservoir thermal conductivity and wellbore radius, etc. It reflects the well's ability to conduct heat.

$$WI^{cond} = 2\pi \sqrt{\lambda_{xx} \lambda_{yy}} \Delta z \big/ \ln \left(r_e^{cond} / r_{bh} \right) \tag{3}$$

where λ_{xx}, λ_{yy} and r_e^{cond} are respectively reservoir thermal conductivity [W·m^{-1}·K^{-1}] in the length direction, reservoir thermal conductivity [W·m^{-1}·K^{-1}] in the width direction and effective wellbore radius for heat conduction [m] which can be calculated by (Shi et al., 2024):

Table 2

Comparison of coupling terms at the wellbore-reservoir interface. The heat exchange calculations at the non-open-hole section interface are compared using the numerical and analytical approaches, and the approach without considering wellbore lateral heat transfer.

Region	Coupling term	Numerical approach	Analytical approach	An approach without considering wellbore lateral heat transfer
Non-open-hole	Energy: q_{EG}^{cp}	$2\pi r_{to} U_{to} \left(T^w - T^{cf} \right) C$ (Willhite, 1967)	$2\pi \lambda^f \left(T^w - T_{fa}^f \right) C / f(t)$ (Ramey Jr, 1962)	0
Open-hole	Mass: q_{MS}^{cp}	$\frac{\rho_l}{\mu} WI^{flow} (p^w - p^r) C$ (Peaceman, 1983)		
	Energy: q_{EG}^{cp}	$\left[\frac{\rho_l}{\mu} WI^{flow} (p^w - p^r) h_l + WI^{cond} (T^w - T^r) \right] C$		

*U means heat transfer coefficient, C is conversion factor and WI represents well index.

$$r_e^{cond} = 0.28 \frac{\sqrt{\sqrt{\lambda_{xx}/\lambda_{yy}}(\Delta x)^2 + \sqrt{\lambda_{yy}/\lambda_{xx}}(\Delta y)^2}}{(\lambda_{xx}/\lambda_{yy})^{1/4} + (\lambda_{yy}/\lambda_{xx})^{1/4}} \tag{4}$$

As for the fluid flow and heat transfer in the radial direction for the non-open-hole section, mass transfer is not considered and only heat exchange exists between the wellbore and surrounding formation. For the non-open-hole section, three calculation approaches for the heat exchange are shown with numerical, analytical and without considering

nearest formation (i.e., T^{cf} where superscript cf is cement/formation interface) and an outside tubing heat transfer coefficient (U_{to}). Both formation temperature and temperature at the interface of cement and formation are dynamic. As shown in Equation (5), the outside tubing heat transfer coefficient is a combination of several thermal resistances including those of the tubing, annulus fluid, casing and cement, which can be referred to in more detail in Willhite (1967) and Xiong et al. (2016).

$$U_{to} = \left[\frac{r_{to}}{r_{ti}\beta_{fft}} + \frac{r_{to}\ln(r_{to}/r_{ti})}{\lambda_t} + \frac{r_{to}\ln(r_{ins}/r_{to})}{\lambda_{ins}} + \frac{r_{to}}{r_{ins}(\beta_{con} + \beta_{rad})} + \frac{r_{to}\ln(r_{co}/r_{ci})}{\lambda_{cas}} + \frac{r_{to}\ln(r_{cf}/r_{co})}{\lambda_{cem}} \right]^{-1} \tag{5}$$

wellbore lateral heat transfer, see Table 2. In the numerical approach, the heat exchange is characterized by the temperature difference between the wellbore (i.e., T^w where subscript w means wellbore) and the

where r_{ti}, r_{to}, r_{ins}, r_{ci}, r_{co} and r_{cf} represent the radii of inside tubing, outside tubing, tubing insulation, inside casing, outside casing and cement/formation interface, respectively. λ_t, λ_{ins}, λ_{cas} and λ_{cem} are the
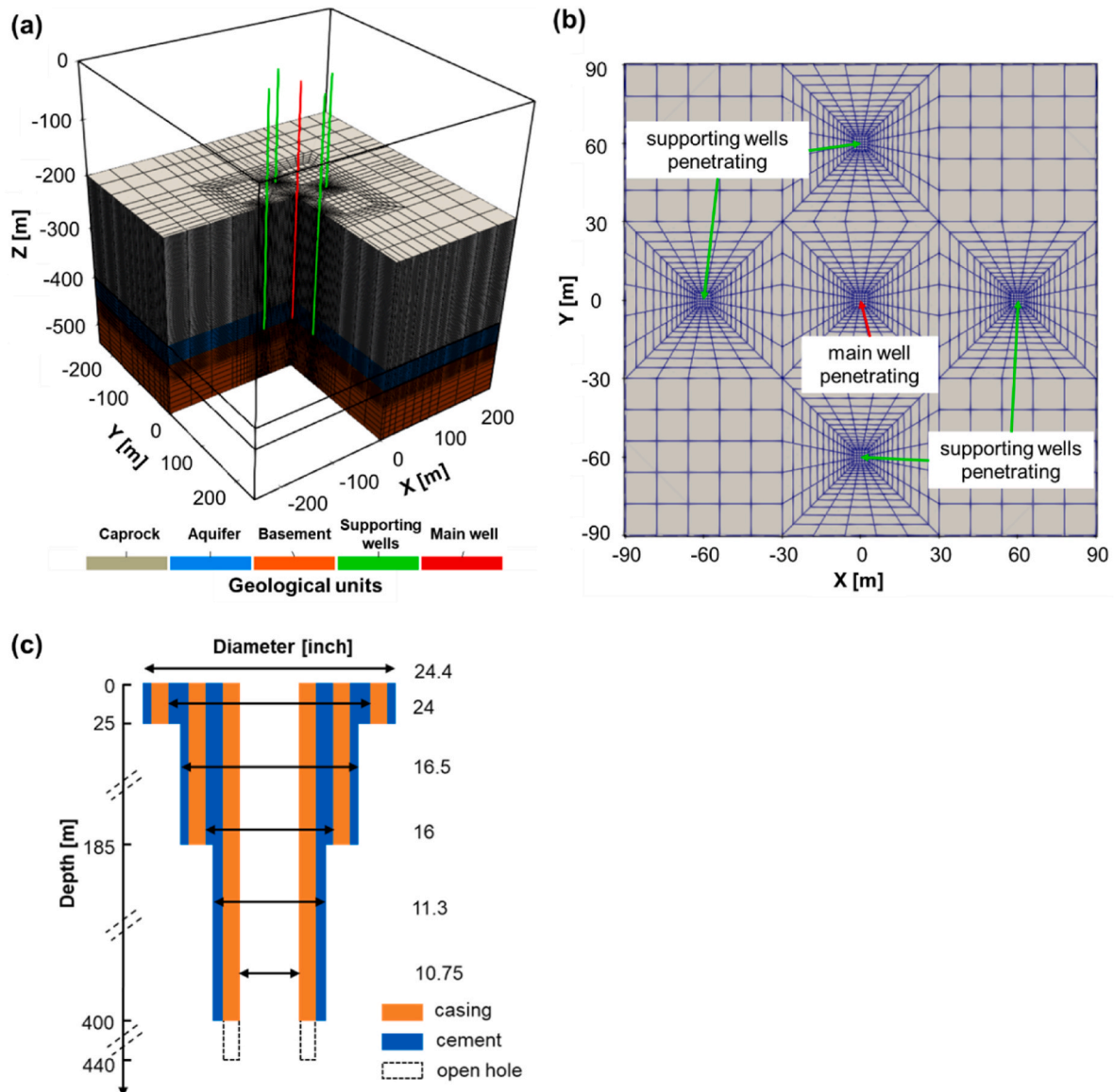

Fig. 1. Schematic representation of (a) a five-spot system for HT-ATES; (b) the top view of the wellbore placement; (c) the geometrical configuration of the wellbore. Note that the main well and supporting wells have the same configuration.

thermal conductivities of the tubing wall, tubing insulation, casing wall and cement. β_{fft}, β_{con} and β_{rad} are the convective heat transfer coefficient between the fluid film in tubing and the tubing wall, and the convective and radial heat transfer coefficients of fluid inside the annulus. The numerical algorithm for solving the coupled wellbore-reservoir model is detailed in Appendix I. Assuming that the far-field formation temperature (T_{fa}^f in Table 2) is constant, the analytical approach only considers the heat transfer between the wellbore and formation but ignores the heat transfer processes between the tubing-casing-cement-formation regions. The comparison of the implemented method and Ramey Jr (1962) analytical solution for the wellbore outlet temperature evolution is shown in Appendix II. The third approach (Table 2) for calculating the heat exchange in the non-open-hole section neglects the wellbore lateral heat transfer.

2.2. Numerical model settings

Inspired by the GeoSwiss Bern Project (Vidal et al., 2022), a five-spot system containing a 3D multi-layer (i.e., caprock, aquifer and basement) HT-ATES system for reservoir and five 1D wellbores, is employed in this study (see Fig. 1 (a)). A 40 m thick aquifer, sandwiched between low-permeable caprock and basement layers, serves as the target zone for thermal energy storage. The whole model, including the formation and wellbore system, spans depths from 0 m to 440 m and the formation extends horizontally from −250 m to 250 m. The aquifer is located at a depth of 400 m–440 m. An unstructured mesh consisting of hexahedral elements was created using GMSH software (Geuzaine and Remacle, 2009). The element size of reservoir grids varies from 1 m near the wellbores to 25 m at boundaries (Fig. 1(a–b)) to balance computational efficiency and numerical accuracy. A finer grid resolution (i.e., $\Delta x = \Delta y = 1$ m) is applied near the wellbores to accurately capture steep thermal and pressure gradients resulting from injection and production processes. This ensures precise wellbore-reservoir heat transfer calculations and reduces numerical dispersion. In contrast, a coarser grid (up to 25 m) is used at the boundaries, where thermal and pressure variations are more gradual, reducing computational cost without compromising solution accuracy. This adaptive meshing strategy optimizes simulation performance while maintaining numerical stability and convergence. The wellbore system comprises one centrally located main well (red color in Fig. 1 (a)) and four supporting wells (green color in Fig. 1 (a)), each symmetrically positioned around the main well at an equal distance of 40 m. For heat storage and extraction in the aquifer, the open-hole section of the wellbore system (located at a depth of 400 m–440 m) allows fluid flow and heat transfer (including both convection and conduction) with the aquifer. In contrast, the non-open-hole section exchanges heat solely through conduction with the surrounding formations. The geometrical configuration of a typical borehole completion within this wellbore system is illustrated in Fig. 1 (c). The wellbore above the open-hole section is cased to ensure stability, with diameters ranging from 10.75 inches (~0.27 m, i.e., r_{bh}) to 24.4 inches (~0.62 m). 0.05 m (i.e., Δz) is used as the mesh size of the wellbore to capture the important dynamics in the flow process. Referring to the realistic and representative data in the GeoSwiss Bern Project, the physical properties of solids (i.e., rock, wellbore cement layer and casing) and fluid are summarized in Tables 3 and 4, respectively. The input data for calculating Equations (1)–(4) in reference case are summarized as follows: 10^{-13} m^2 (reservoir permeabilities in the length direction (k_{xx}) and width direction (k_{yy}), Table 3), 2 W m^{-1} K^{-1} (reservoir thermal conductivities in the length direction (λ_{xx}) and width direction (λ_{yy}), Table 3), 1 m (length and width of a grid block), 0.05 m (depth of a grid block) and 0.27 m (wellbore radius (r_{bh})).

For the initial temperature condition, the ground surface temperature is assumed to be 20 °C, and the subsurface temperature follows the general geothermal gradient of 0.03 °C•m^{-1}. The initial pressure distribution takes the hydrostatic gradient 9.81•10^3 Pa m^{-1}. Regarding the reservoir boundary conditions, a constrained temperature distribution (same as initial) and no fluid flow boundaries are applied at the four vertical sides (including the front, back, left and right sides), while the top (i.e., ground surface) and the bottom of the model are set with closed boundaries for both heat energy and fluid flow. One complete heat storage and extraction cycle takes one year. During the heat storage phase (nine months), 90 °C hot fluid is pumped into the reservoir with an injection rate of 25 L s^{-1} through the main well while four supporting wells produce fluid with the constrained wellhead pressure of 1 bar. In the following three months, the injection and production schemes are reversed for the heat extraction phase. During this period, 50 °C liquid (water) is injected with 6.25 L s^{-1} through each supporting well and fluid can be freely produced from the main well (wellhead pressure 1 bar). Note that there is a considerable compression effect on the fluid density due to pressure variation in the system, such as pressure build-up between the main wellbore and supporting wellbores. We perform five cycles in this study, taking a total time of five years. The operational time for injecting and producing hot fluid can be influenced by factors such as local climate conditions, heating demand, etc. (Sheldon et al., 2021; Beernink et al., 2024). The nine months for heat storage and three months for heat extraction are chosen just for demonstration purposes. The operational schedule is summarized in Table 5. Furthermore, the preliminary grid resolution, numerical scheme, and convergence tests confirm minimal numerical diffusion, the numerical solution remains reliable for capturing transient wellbore-reservoir heat transfer.

2.3. Performance indicators of the HT-ATES system

The performance of the HT-ATES system is evaluated based on four annual performance indicators: energy recovery efficiency, extracted energy, wellbore lateral heat transfer fraction and reservoir heat loss

Table 4
Fluid properties in the reservoir and wellbore systems (L. Smith and Chapman, 1983).

Properties	Symbols	Units	Value
Bulk modulus	K_l	Pa	$2\cdot10^{10}$
Density	ρ_l	kg m^{-3}	$\rho_l = 1000\cdot e^{\frac{p}{K_l}}$
Viscosity	μ	Pa s	$\mu = 2.4\cdot10^{\left(\frac{248.37}{T-140}-5\right)}$
Specific heat capacity	$C_{p,l}$	J kg^{-1} K^{-1}	4000
Thermal conductivity	λ_l	W m^{-1} K^{-1}	0.6

Table 3
Rock properties of the reservoir and wellbore systems (Wilkins et al., 2021; Vidal et al., 2022; Brown and Falcone, 2024).

Properties	Symbols	Units	Reservoir system			Wellbore system	
			Caprock	Aquifer	Basement	Cement	Casing
Porosity	φ	-	0.01	0.25	0.01	-	-
Permeability	k	m^2	10^{-16}	10^{-13}	10^{-16}	-	-
Density	ρ^s	kg m^{-3}	2600	2600	2600	-	-
Specific heat capacity	c_p^s	J kg^{-1} °K^{-1}	850	850	850	-	-
Thermal conductivity	λ^s	W m^{-1} °K^{-1}	2	2	2	1.1	45
Roughness	f	m	–	–	–	–	10^{-4}

Table 5
Summary of the operational schedule.

Cycle Phase	Duration (months)	Main Well	Injection temperature (°C)	Injection flow rate (L/s)	Supporting Wells	Injection temperature (°C)	Injection flow rate (L/s)
Heat storage	9	Injection	90	25	Production	/	/
Heat extraction	3	Production	/	/	Injection	50	6.25 (each)

fraction. Furthermore, wellbore lateral heat transfer is defined in two ways: (1) *wellbore lateral heat loss*, which occurs when heat transfers from the wellbore to the surrounding formation; (2) *wellbore lateral heat gain*, which occurs when heat transfers from the formation to the wellbore. In our case, the wellbore lateral heat loss to the formation is greater than the lateral heat gain from the formation due to the higher temperature difference during the heat storage phase compared to the extraction phase. Specifically, during storage, the injection fluid (90 °C) has a much higher temperature than the surrounding formation (~33.2 °C at 400 m depth), resulting in significant conductive heat loss. In contrast, during extraction, the injection temperature (50 °C) is much closer to the formation temperature, leading to the wellbore's relatively lower heat gain. Therefore, for simplicity, we use the *net wellbore heat loss* (defined as the amount of 'wellbore heat loss' minus 'wellbore heat gain') to represent the annual lateral heat transfer of the wellbore. The classification of the main and supporting wells depends on the operational phase: the main well is an injection well and supporting wells are production wells in the heat storage stage; for the heat extraction stage, the main well becomes a production well and supporting wells are injection wells. The definitions of relevant parameters are summarized as follows.

The energy recovery efficiency (η) (Doughty et al., 1982) equals to:

$$\eta = \frac{E_{ext}}{E_{inj}} \tag{6}$$

where E_{ext} and E_{inj} are the extracted energy and the injected energy, respectively.

The extracted energy (E_{ext}) can be calculated by:

$$E_{ext} = \int_0^t c_l |Q_{ext}| (\rho_{ext} T_{ext} - \rho_0 T_0) dt \tag{7}$$

where t, c_l, ρ_{ext}, Q_{ext}, T_{ext}, ρ_0 and T_0 are time [s], specific heat capacity [J•kg^{-1}•K^{-1}] of liquid, liquid density [kg•m^{-3}], total extraction flow rate [m^3•s^{-1}] and temperature [K] at extraction wellhead, initial liquid density [kg•m^{-3}] and initial liquid temperature [K] in the reservoir, respectively.

Meanwhile, the injected energy (E_{inj}) is:

$$E_{inj} = \int_0^t c_l |Q_{inj}| (\rho_{inj} T_{inj} - \rho_0 T_0) dt \tag{8}$$

where ρ_{inj}, Q_{inj} and T_{inj} are injection liquid density [kg•m^{-3}], total injection flow rate [m^3•s^{-1}] and injection liquid temperature [K] at the wellhead, respectively.

Furthermore, according to the energy consumption types of the injected energy (E_{inj}), it can be divided into the extracted energy (E_{ext}), wellbore lateral heat loss (E_{los_w}) and reservoir heat loss (E_{los_r}).

$$E_{inj} = E_{ext} + E_{los\_w} + E_{los\_r} \tag{9}$$

The four terms in Equation (9) are interrelated, meaning that one of these terms can be obtained if the other three are known. According to the heat transfer flux between the wellbore and formation in the non-open-hole section (as shown in Table 2), the wellbore lateral heat loss ($E_{los\_w}^{num}$) from numerical approach can be obtained from:

$$E_{los\_w}^{num} = \int_0^t \int_0^{L_w} 2\pi r_{to} U_{to} (T^w - T_{ne}^f) dz dt \tag{10}$$

where L_w is the wellbore length, superscript f and subscript ne are the formation and nearest node of the corresponding reservoir grid, respectively.

Similarly, the wellbore lateral heat loss ($E_{los\_w}^{ana}$) from the analytical approach is:

$$E_{los\_w}^{ana} = \int_0^t \int_0^{L_w} 2\pi \lambda^f \left(T^w - T_{fa}^f\right) dz dt \tag{11}$$

where subscript fa represents far-field.

The wellbore lateral heat loss fraction α_{los_w} can be obtained from:

$$\alpha_{los\_w} = \frac{E_{los\_w}}{E_{inj}} \tag{12}$$

where E_{los_w} is $E_{los\_w}^{num}$ in the numerical approach or $E_{los\_w}^{ana}$ in the analytical approach.

Thus, the reservoir heat loss fraction α_{los_r} equals to:

$$\alpha_{los\_r} = 1 - \eta - \alpha_{los\_w} \tag{13}$$

E_{los_r} represents energy lost from the injected fluid into the surrounding rock formations (such as caprock and basement layers) via conductive **heat transfer**. This loss is because when hot fluid is injected into the reservoir, part of the heat is conducted from the reservoir to adjacent formations that are not directly involved in heat recovery. Heat loss through the boundaries of the model (e.g., caprock or basement layers) is assumed to occur via vertical conductive transfer, since the model boundaries are considered adiabatic (no heat flow) in the lateral direction.

3. Results and discussions

In this part, we first present the behavior of a reference case for the HT-ATES, including the temperature distributions and performance evaluation of the HT-ATES system. Following this, to reveal the impact of wellbore lateral heat loss on HT-ATES performance, we perform a parameter sensitivity analysis of key factors, including wellbore configurations (wellbore diameter, casing thermal conductivity and number of supporting wells) and operational parameters (injection flow rate and injection temperature at the main well).

3.1. Reference case

3.1.1. Temperature distributions

Temperature distributions within the aquifer, its surrounding formations and the formations around the wellbore are depicted in Fig. 2 (a) at four key times: at the end of the first storage (0.75 years, subplot a1), at the end of the first extraction (1 year, marking the completion of the first full cycle, subplot a2), at the end of the fifth storage (4.75 years, subplot a3) and at the end of the fifth extraction (5 years, marking the completion of the fifth full cycle, subplot a4). Each storage period involves injecting 90 °C hot fluid, leading to continuous heating of the aquifer and its overlying and underlying formations (Fig. 2 (a1) and (a3)). During the extraction phase, hot fluid is withdrawn from the main well at the center of the model, resulting in an I-shaped temperature distribution in the aquifer and its adjacent overlying and underlying formations. This pattern becomes more pronounced with an increasing
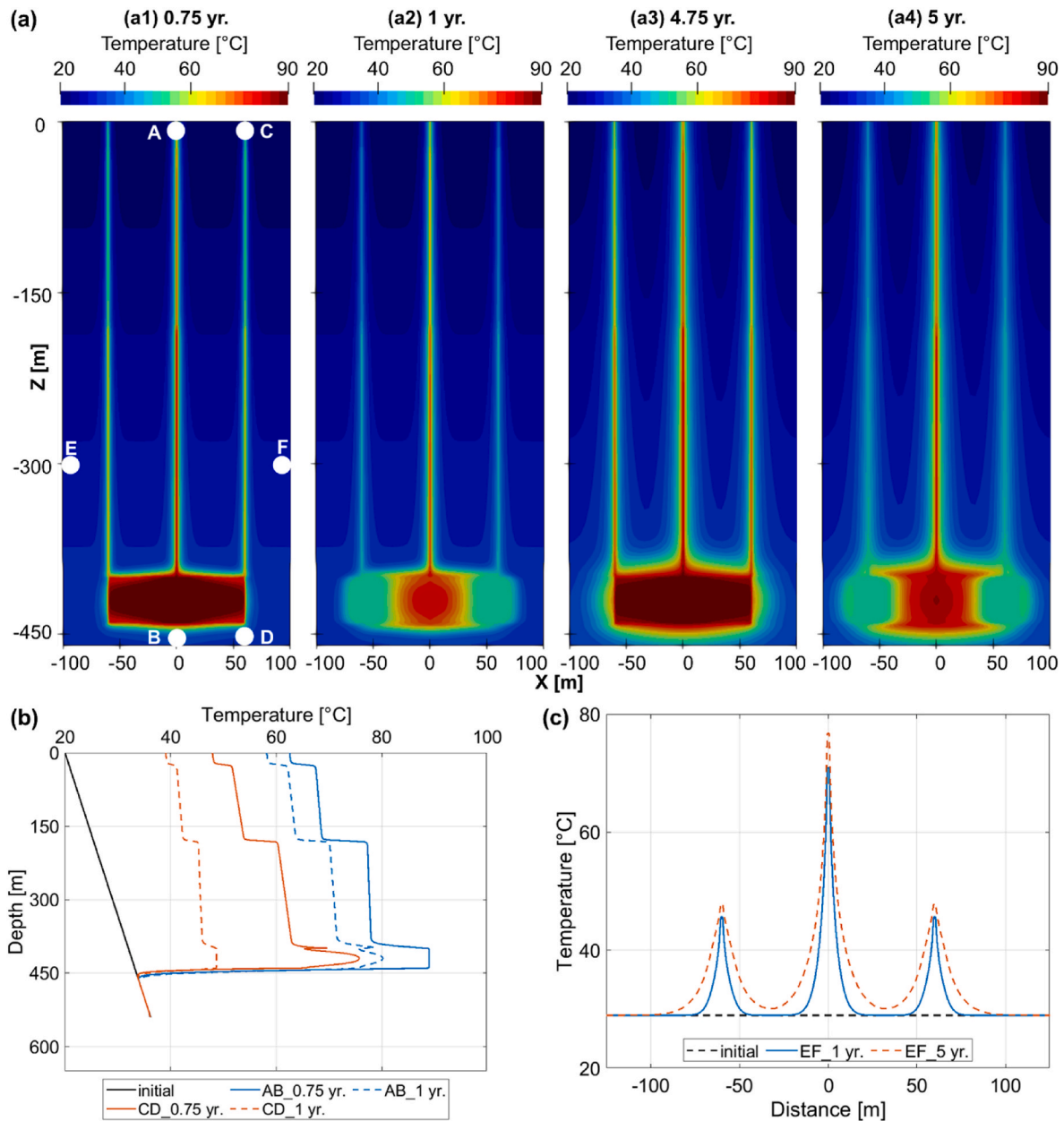
Fig. 2. Numerical results of the reference case, including the temperature distributions in the aquifers and formations at (a1) 0.75 years; (a2) 1 year; (a3) 4.75 years; (a4) 5 years; (b) vertical temperature profile along lines A-B and C-D across the entire model; and (c) horizontal temperature profile along line E-F at a depth of 300 m across the entire model.

number of complete heat storage and extraction cycles (Fig. 2 (a2) and (a4)). The observed phenomenon occurs because the overlying and underlying formations are heated by conduction from the hot fluid injected into the aquifer. While the hot fluid is produced from the main well during the extraction time, the temperatures in the high-temperature zones of both the aquifer and its surrounding formations decrease. However, the overlying and underlying formations lose heat through conduction, which is slower compared to the convective heat transfer in the aquifer. Consequently, there is a delayed temperature response in the overlying and underlying formations compared to the aquifer.

Around the non-open-hole section of the wellbores, wellbore lateral heat loss to the surrounding formations causes their temperatures to rise, with the increase becoming more pronounced with depth (Fig. 2 (b)). This intensified temperature rise with depth is due to the weak insulation of the wellbore as the number of insulation layers decreases.

Specifically, there are three insulation layers from 0 to 25 m depth, two insulation layers from 25 m to 185 m depth and one insulation layer from 185 m to 400 m depth (Fig. 1 (c)) in the non-open-hole section of the wellbores. By comparison, in the open-hole sections (i.e., from 400 m to 440 m depth), the aquifer experiences a greater temperature increase compared to the formations around the non-open-hole sections of the wellbores. This occurs because the convective heat transfers due to fluid flow in the open-hole section, combined with heat conduction, results in more effective heat transfer compared to the pure heat conduction occurring around the non-open-hole sections of the wellbores. The abnormal temperature peak near ~400 m (see curves AB at 1 yr and CD at 0.75 yr in Fig. 2(b)) occurs in the water production well due to differing heat transfer mechanisms: convection and conduction in the open-hole section versus conduction alone in the non-open-hole section. As hot fluid is extracted, heat from the aquifer transfers to the wellbore. However, due to heat loss at the boundaries, the central temperature is
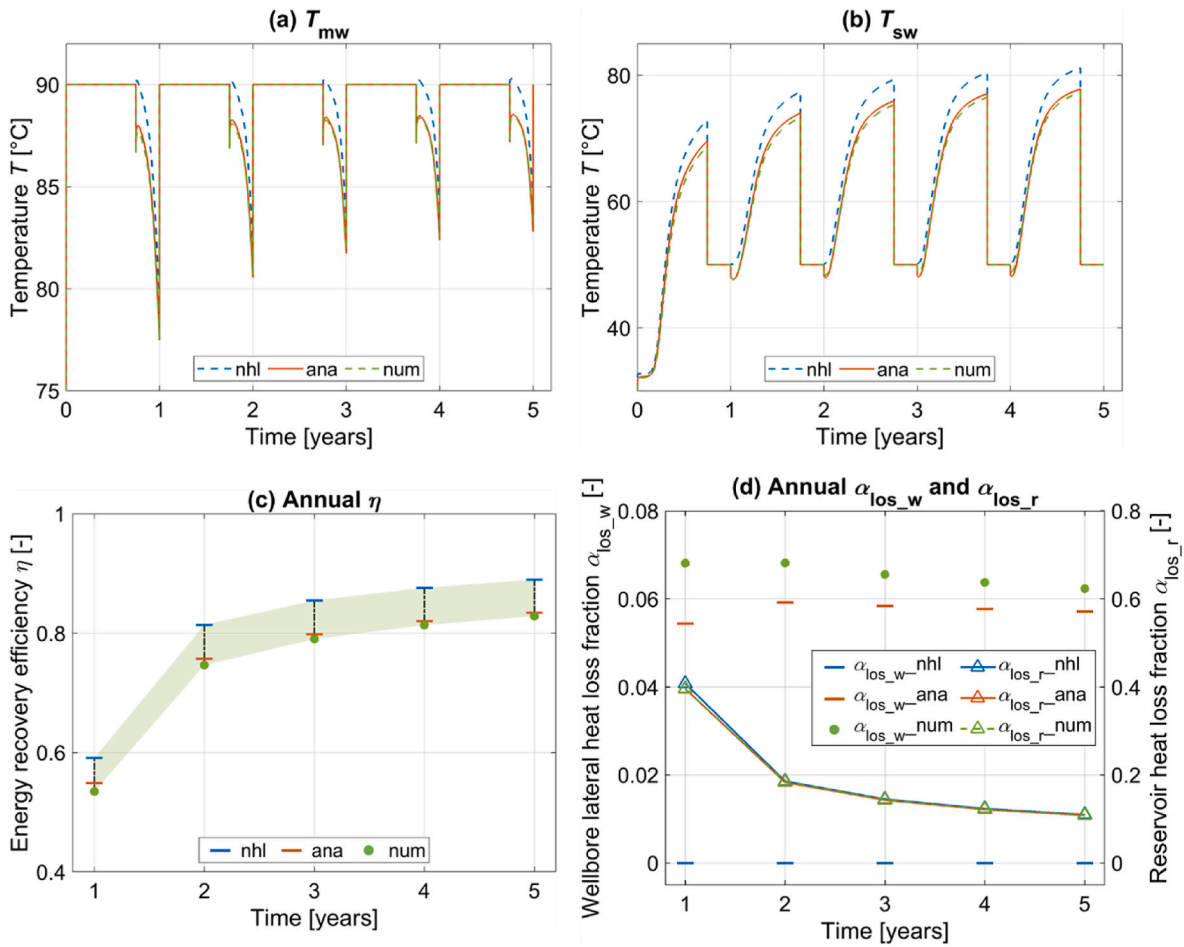
Fig. 3. Comparison of numerical (num) and analytical (ana) results for cases with and without considering wellbore lateral heat loss (nhl: no heat loss) on the performance indicators of the HT-ATES system: (a) temperature at the main wellhead; (b) temperature at the supporting wellhead; (c) annual energy recovery efficiency; (d) annual wellbore lateral heat loss fraction (left y-axis) and reservoir loss fraction (right y-axis). Green symbols represent results from the numerical approach; orange symbols indicate the analytical solution; blue symbols show results where wellbore lateral heat transfer is ignored. The α_{los_w} and α_{los_r} mean wellbore lateral heat loss fraction [-] and reservoir heat loss fraction [-], respectively. (For interpretation of the references to color in this figure legend, the reader is referred to the Web version of this article.)

expected to be higher, resulting in a peak temperature at the center. Meanwhile, the varying injection temperatures (90 °C compared to 50 °C) and durations (9 months compared to 3 months) of the fluid during the heat storage and heat extraction phases alter the temperature distribution in the wellbore and surrounding formation. The combination of these factors results in a localized temperature peak at the interface between the open-hole and non-open-hole sections of the water production well. Additionally, the horizontal extent of lateral heat propagation (Fig. 2 (c)) around the non-open-hole sections of the wellbores expands due to the continuous heating from the wellbore to the surrounding formations. This effect becomes more pronounced as the number of complete heat storage and extraction cycles accumulates over time (Equation (10)).

3.1.2. Performance indicators

The fluid temperatures at the wellheads of the main and supporting wells are shown in Fig. 3(a–b). The temperatures calculated using the analytical approach and the approach that ignores wellbore are higher than those obtained from the numerical approach. For instance, at 0.75 years, the temperature at the supporting wellhead (T_{sw}) is 0.8 °C higher using the analytical approach and 4.2 °C higher using the approach without considering wellbore lateral heat transfer compared to the temperature obtained using the numerical approach (68.7 °C see Fig. 3 (b)). These discrepancies respectively arise from the steady-state heat

transfer between the wellbore and formation in the analytical approach and the neglect of heat exchange between the wellbores and their surrounding formations in the third approach.

To assess the HT-ATES performance of the reference case, we use energy recovery efficiency (Fig. 3 (c)), wellbore lateral heat loss fraction (Fig. 3 (d)) and reservoir heat loss fraction (Fig. 3 (d)) as performance indicators. Since the amount of injected energy remains constant and the extracted energy is directly proportional to energy recovery efficiency (as shown in Equation (6)), variations in extracted energy can be inferred directly from changes in energy recovery efficiency. Therefore, the extracted energy is not discussed respectively here. The annual energy recovery efficiency (Fig. 3 (c)) in the first year, calculated by the numerical approach (53.6 %), is lower than that obtained using the analytical approach (55 %) and the approach that disregards wellbore lateral heat loss (59.2 %). The low energy recovery efficiencies in the first year are primarily due to the high reservoir heat loss (Fig. 3 (d)), which is driven by the large temperature difference between the injected hot fluid and the initial reservoir temperature. Specifically, the reservoir heat loss fractions calculated by the numerical and analytical approaches, and the approach without considering wellbore lateral heat transfer are 39.59 %, 39.57 % and 40.8 %, respectively. As heat storage and extraction cycles accumulate over time, the reservoir heat loss fraction gradually decreases, reaching approximately 11 % by the fifth year. This reduction in heat loss leads to a significant improvement in

energy recovery efficiency, which increases by about 30 %, surpassing 80 % by the fifth year. Fig. 3 (d) shows the wellbore lateral heat loss fraction obtained using the numerical approach, which reaches a maximum of 6.8 % in the second year. This is higher than the 5.9 % calculated from the analytical approach and the 0 % from the approach without considering wellbore lateral heat transfer. The lateral heat loss

calculated using the analytical approach is 13 % lower than that obtained from the numerical approach. After the second year, wellbore lateral heat loss decreases as the surrounding formations heat up, reducing the temperature difference and consequently, the amount of heat lost as described by Equations (10) and (11). This decline in wellbore lateral heat loss further contributes to the improvement in energy
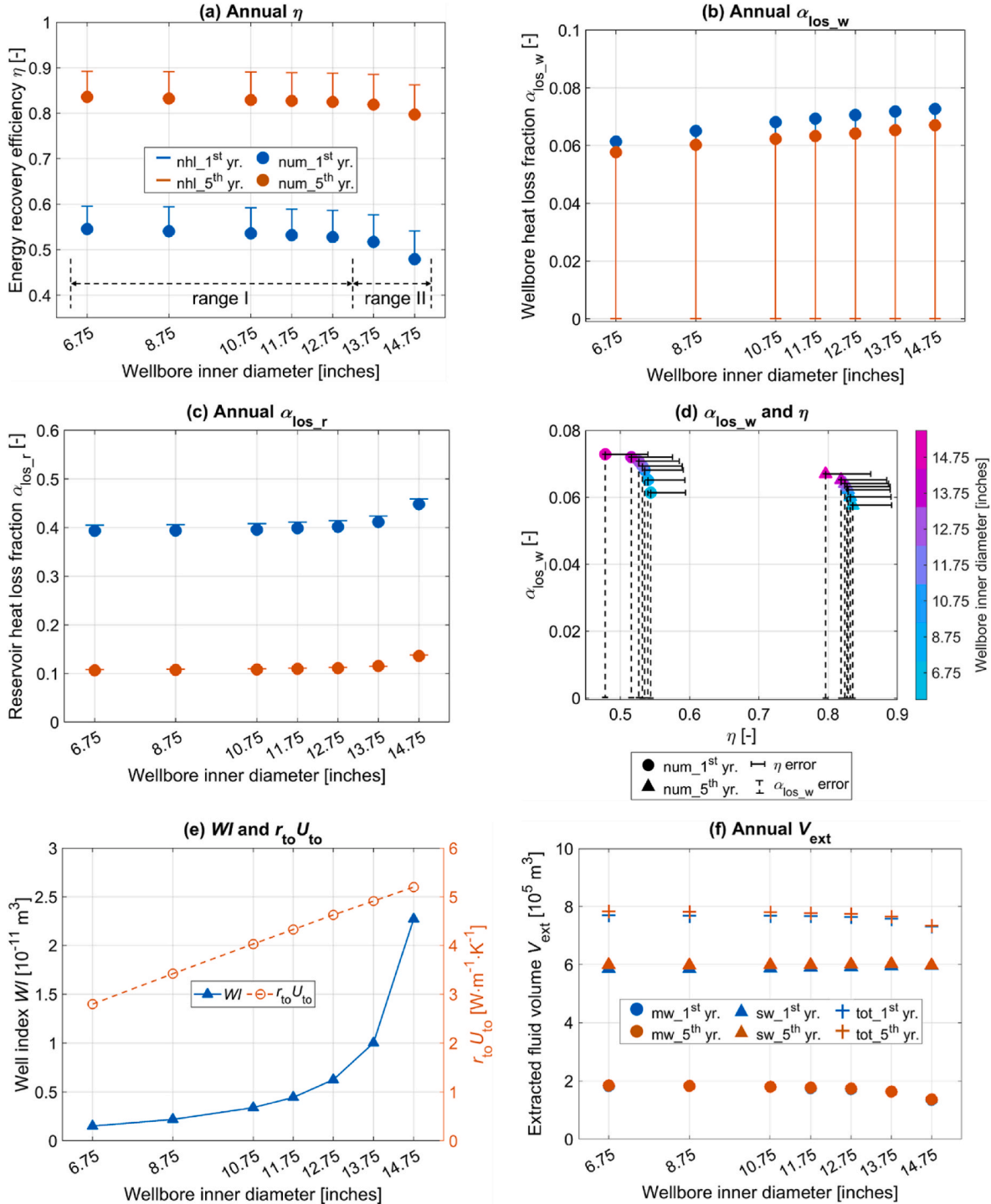
Fig. 4. Effects of wellbore diameter on annual (a) energy recovery efficiency; (b) wellbore lateral heat loss fraction; (c) reservoir heat loss fraction; (d) wellbore lateral heat loss fraction versus annual energy recovery efficiency from the numerical approach at 1st and 5th year. The horizontal and vertical error bars mean the differences between the numerical approach and the approach without considering wellbore lateral heat transfer in annual energy recovery efficiency and wellbore lateral heat loss fraction, respectively; (e) WI in open-hole section and $r_{to}U_{to}$ of non-open-hole section at 200 m depth; (f) annual extracted fluid volumes from the main well, supporting wells, and the total volume, as calculated using the numerical approach. The inner diameter of the wellbore in the reference case is 10.75 inches.

recovery efficiency.

The numerical approach is the most accurate, as it captures complex heat exchange processes between the wellbore and surrounding formations, along with dynamic temperature variations in far-field formations. In contrast, the analytical approach and the approach that neglects wellbore lateral heat transfer tend to overestimate fluid temperature and energy recovery efficiency due to simplifying assumptions.

While the analytical approach reduces the running time of one simulation from ~46.5 h (numerical approach) to ~44.5 h using 152 CPU cores, this gain comes at the expense of accuracy, particularly in capturing detailed thermal interactions and wellbore lateral heat loss. Although the analytical method can approximate general trends over time, such as improvements in energy recovery and decreases in wellbore lateral heat losses, the numerical approach remains essential for high-precision applications including system optimization and minimizing heat losses, as it can accurately model complex dynamics and provide reliable long-term performance predictions.

3.2. Effects of wellbore configurations

3.2.1. Wellbore diameter

We evaluate seven wellbore diameter sets of main and supporting wellbores, with inner diameters ranging from 6.75 inches (4 inches smaller than the reference case) to 14.75 inches (4 inches larger than the reference case), with four intermediate inner diameters of 8.75, 11.75, 12.75 and 13.75 inches. The outer geometry of the entire wellbore remains constant across all depths. The energy recovery efficiency (Fig. 4 (a)) decreases as the wellbore diameter increases, while both the wellbore lateral heat loss fraction (Fig. 4 (b)) and reservoir heat loss fraction (Fig. 4 (c)) show the opposite trend. When the wellbore inner diameter increases from 6.75 inches to 12.75 inches (range I), the changes in annual energy recovery efficiency and reservoir heat loss fraction are gradual and linear, with only minor variations. In contrast, a further increase in wellbore diameter, from 13.75 inches to 14.75 inches (range II), results in more significant changes, as depicted in Fig. 4(a–b). The wellbore lateral heat loss fraction, however, changes throughout the entire range of diameters (Fig. 4 (b)). The diminished differences in the ranges and variations of energy recovery efficiency and wellbore lateral heat loss fraction between the numerical approach and the approach without considering wellbore lateral heat transfer, influenced by changes in wellbore diameter, are summarized from the 1st to the 5th year in Fig. 4 (d). From the 1st to the 5th year, the case with a large inner diameter of 14.75 inches consistently demonstrates low energy recovery efficiency and high wellbore lateral heat loss compared to the other cases, which exhibit only minor and smooth variations.

These trends can be explained as follows. According to Equation (1), with constant reservoir characteristics and grid size, a large wellbore diameter owns a high *WI* value (Fig. 4 (e)). This indicates that, for the same injection flow rate, a large wellbore diameter leads to small pressure build-up around the injection area in the aquifer. The combination of less initial fluid production due to reduced pressure build-up, followed by increased production as the system stabilizes and reservoir pressure field stabilizes, and the eventual equalization of production rates, leads to a net increase in total fluid production from the supporting wells with large wellbore diameters (see Fig. 4 (f) and A3 (a) in Appendix III). During the extraction phase, the main well with a larger diameter experiences consistently lower pressure levels than the smaller diameter cases (A3 (d) in Appendix III). The pressure increase is slow in the large diameter case due to reduced flow resistance, which results in a weak pressure gradient between the reservoir and the well. As a result, the driving force for fluid movement from the reservoir into the main well is diminished. Because the pressure at the main well is lower, the extraction rate of fluid from the reservoir is significantly reduced. This diminished pressure gradient leads to a substantial decrease in the volume of fluid produced from the main well. The combination of low pressure and a slow pressure response means that, during the extraction

phase, the main well with a larger diameter produces considerably less fluid compared to smaller diameters. Consequently, despite large wellbore diameters leading to great fluid production in the heat storage phase, the associated decrease in heat storage due to low pressures and weak gradients results in a low net annual fluid production when compared to small diameters (Fig. 4 (f)). The reduced fluid extraction volumes result in less energy carried by the extracted fluid. As a result, the energy recovery efficiency (Fig. 4 (a)) decreases, and there is more heat loss in the reservoir (Fig. 4 (c)). Additionally, a large wellbore diameter increases the lateral heat exchange area with the surrounding formations, which linearly increases the values of $r_{to}U_{to}$ in Equation (10) (Fig. 4 (e)). Meanwhile, under the assumption of a constant flow rate, a larger wellbore diameter results in a lower fluid velocity, increasing residence time and enhancing heat loss. However, the lower surface-area-to-volume ratio also reduces conductive heat loss per unit volume, creating a competing effect. Thus, the case with large wellbore diameter result in a high wellbore lateral heat loss fraction (Fig. 4 (b) and (d)), further reducing the energy recovery efficiency. These changes favor the wellbore diameter set case with a 6.75 inches inner diameter, which demonstrates good performance (Fig. 4 (d)). However, it is important to consider that small wellbore diameter may generates high wellbore pressure drops thus increasing the energy consumption for pumps. Therefore, it is crucial to balance these factors and optimize the wellbore diameter based on specific geological conditions, design requirements and heating demands of the system.

3.2.2. Casing thermal conductivity

In the HT-ATES systems, the thermal conductivity (Equation (5)) and cost of casing materials play a critical role in determining the system's thermal performance, operational longevity and overall efficiency. The casing thermal conductivity (Fig. 1 (c)) represents the ability of the casing material to transfer heat between the fluid inside the wellbore and the surrounding formation. Common materials (Pribnow and Sass, 1995; Anwar et al., 2019; Mohammed et al., 2019; Wiktorski et al., 2019) used for wellbore casings include carbon steel (45–60 W m^{-1}•K^{-1}), stainless steel (15–30 W m^{-1}•K^{-1}), PVC (polyvinyl chloride, ~0.19 W m^{-1}•K^{-1}), HDPE (high-density polyethylene, ~0.48 W m^{-1}•K^{-1}) and fiberglass (~0.04 W m^{-1}•K^{-1}). In this example, we consider eight different thermal conductivities (ranging from 0.045–45 W m^{-1}•K^{-1}) of wellbore casing to assess their impact on the performance of the HT-ATES system. Note that only the wellbore casing thermal conductivity is varied, while all other parameters remain consistent with the reference case.

The clear distinction in annual energy recovery efficiency, wellbore lateral heat loss fraction and reservoir heat loss fraction, obtained using the numerical approach and the approach that excludes wellbore lateral heat transfer, is displayed in Fig. 5(a–c) for different casing thermal conductivity cases. The energy recovery efficiency (Fig. 5 (a)) increases as wellbore casing thermal conductivity decreases due to the reduced wellbore lateral heat loss fraction (Fig. 5 (b)). The minimum casing thermal conductivity of 0.045 W m^{-1}•K^{-1} behaves better than other cases by decreasing the annual wellbore lateral heat loss fraction to 3.3 % (i.e., removing ~51.4 % of that in the reference case) and increasing the annual energy recovery efficiency by 3 % than the reference case at the 1st year. From the 1st to the 5th year, the reduced differences in energy recovery efficiency and wellbore lateral heat loss fraction, influenced by changes in casing thermal conductivity, are highlighted when comparing the numerical approach to the approach without considering wellbore lateral heat transfer, as summarized in Fig. 5 (d). The magnitudes of the error bars for energy recovery efficiency and wellbore lateral heat loss fraction between the numerical approach and the approach that excludes wellbore lateral heat transfer increase as the casing thermal conductivity rises. The linear relationship between the variations in energy recovery efficiency and wellbore lateral heat loss fraction with changes suggests that casing thermal conductivity negatively impacts efficiency in a linear manner by changing wellbore lateral
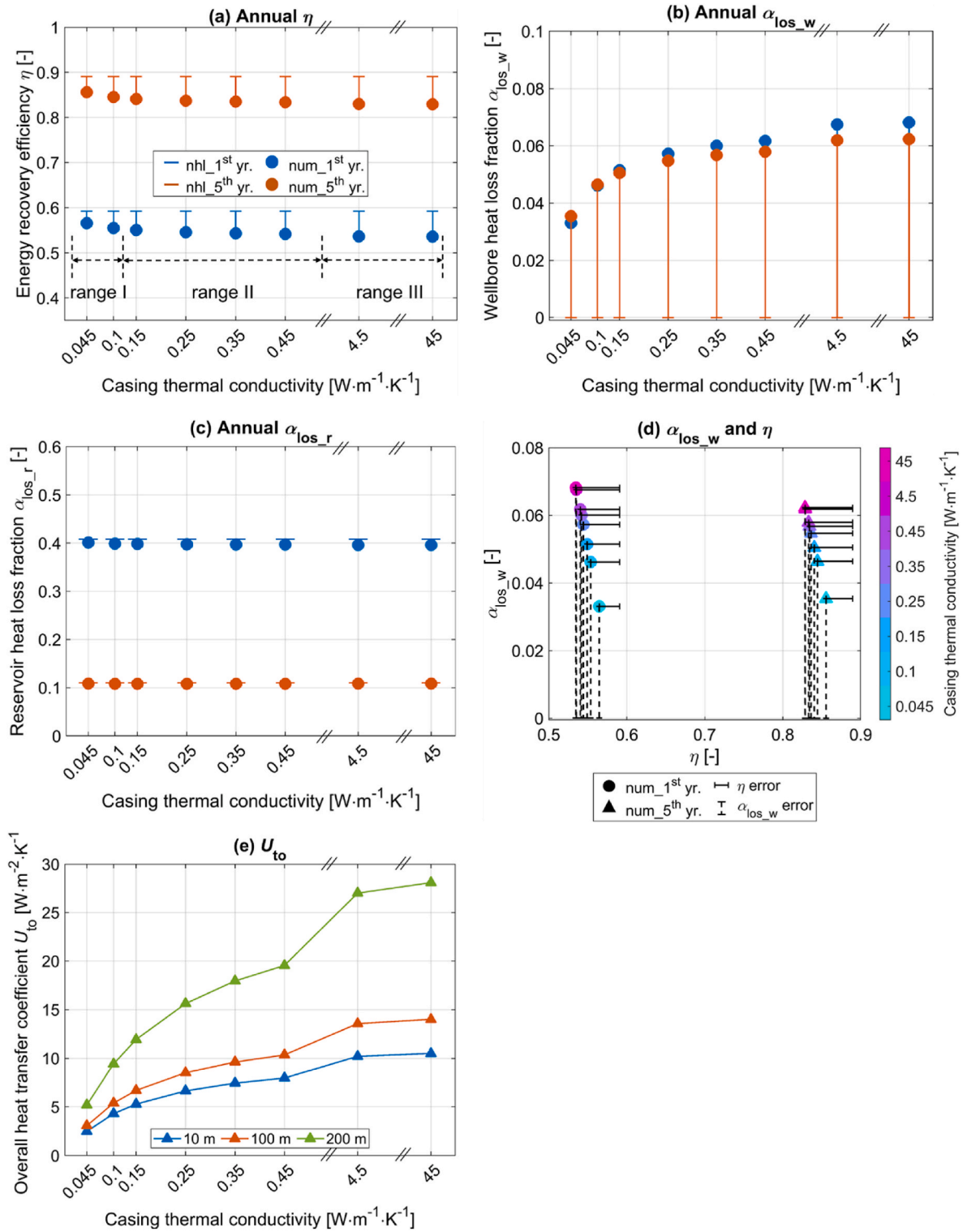
Fig. 5. Effects of wellbore casing thermal conductivity on the annual (a) energy recovery efficiency; (b) wellbore lateral heat loss fraction; (c) reservoir heat loss fraction; (d) wellbore lateral heat loss fraction versus annual energy recovery efficiency from the numerical approach at 1st and 5th year. The horizontal and vertical error bars mean the differences between the numerical approach and the approach without considering wellbore lateral heat transfer in annual energy recovery efficiency and wellbore lateral heat loss fraction, respectively; (e) U_{to} of non-open-hole section at 10 m, 100 m and 200 m, respectively. The casing thermal conductivity in the reference case is 45 W m^{-1}•K^{-1}.

heat loss. The variations within each of the ranges are smooth and small, however, significant differences are observed among them. The explanations are as follows: according to Equation (10), a high wellbore casing thermal conductivity results in an increased U_{to} value (Fig. 5 (e)) with three obvious variation ranges (i.e., 0.045–0.1 W m^{-1}•K^{-1};

0.15–0.45 W m^{-1}•K^{-1}; 4.5–45 W m^{-1}•K^{-1}), which in turn leads to great wellbore lateral heat loss fraction (Fig. 5 (b)) and consequently reduces the energy recovery efficiency (Equation (6) and Fig. 5 (a)). As shown in Fig. 5 (d), low thermal conductivity materials enhance thermal performance by reducing wellbore lateral heat loss fraction. Although high
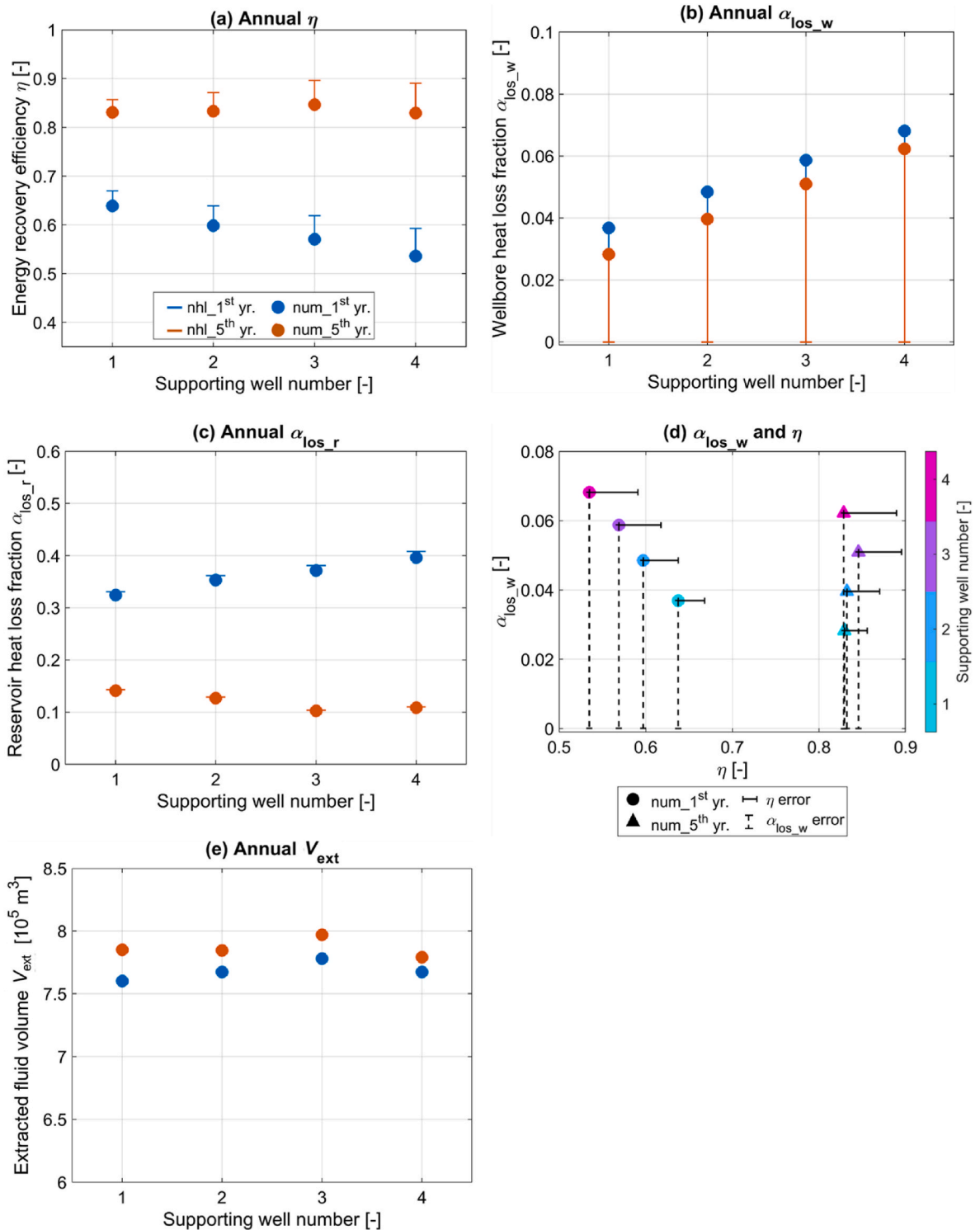
Fig. 6. Effects of number of supporting wells on the annual (a) energy recovery efficiency; (b) wellbore lateral heat loss fraction; (c) reservoir heat loss fraction; (d) wellbore lateral heat loss fraction versus annual energy recovery efficiency from the numerical approach at 1st and 5th year. The horizontal and vertical error bars mean the differences between the numerical approach and the approach without considering wellbore lateral heat transfer in annual energy recovery efficiency and wellbore lateral heat loss fraction, respectively; (e) extracted fluid volumes from the main well, supporting wells and the total volume, as calculated using the numerical approach. The number of supporting wells in the reference case is 4.

HT-ATES system performance requires low casing thermal conductivity, the high cost of selecting casing materials with low thermal conductivity must also be considered, necessitating economic analysis and related optimization.

3.2.3. Number of supporting wells

In the following analysis, we investigate the effects of varying the number of supporting well — specifically 1, 2, 3 and 4 — on the HT-ATES system's performance. All other parameters, including the total injection flow rate, are kept consistent with those of the reference case. The resulting annual energy recovery efficiency, wellbore lateral heat

loss fraction and reservoir heat loss fraction are shown in Fig. 6(a–c). In the first year, the energy recovery efficiency (Fig. 6 (a)) decreases as the number of supporting wells increases, while the reservoir heat loss fraction (Fig. 6 (c)) exhibits the opposite trend. By the fifth year, the case with three supporting wellbores demonstrates the highest energy recovery efficiency and the lowest reservoir heat loss fraction compared to the other cases. Additionally, the total wellbore lateral heat loss fraction increases with the number of supporting wells, as heat loss from both the main and supporting wells contributes to the overall system efficiency.

The reduced differences in the ranges and variations of energy recovery efficiency and wellbore lateral heat loss fraction, influenced by changes in wellbore diameter, are compared between the numerical approach and the approach excluding wellbore lateral heat transfer from the 1st to the 5th year (Fig. 6 (d)). The magnitudes of the error bars for energy recovery efficiency and wellbore lateral heat loss fraction between the numerical approach and the approach that excludes wellbore lateral heat transfer increase with the rise of number of supporting wells.

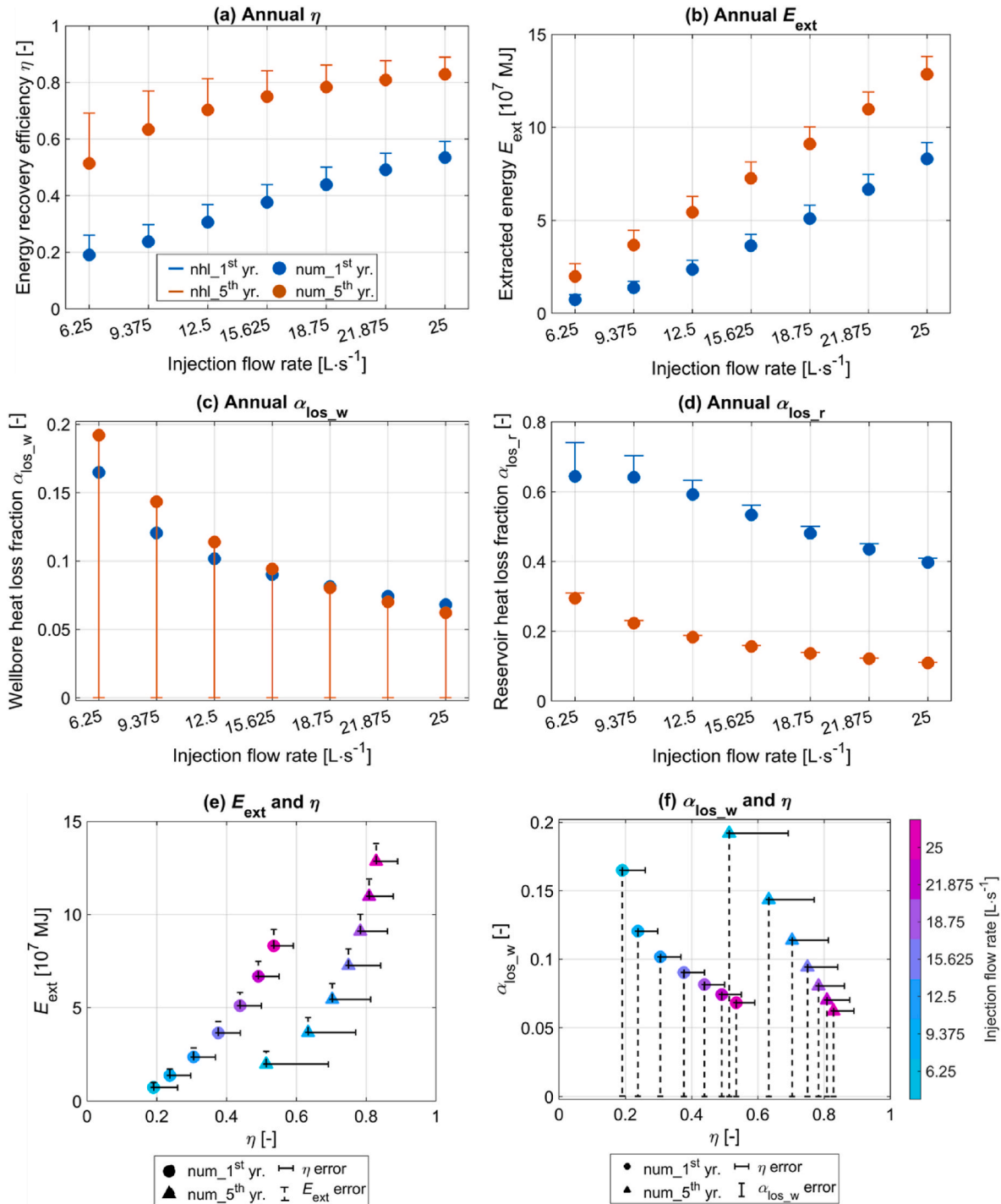The volume of heat storage space is directly proportional to the

Fig. 7. The impact of injection flow rate on the annual (a) energy recovery efficiency; (b) extracted energy; (c) wellbore lateral heat loss fraction; (d) reservoir heat loss fraction; (e) extracted energy versus energy recovery efficiency, and (f) wellbore lateral heat loss fraction versus energy recovery efficiency from the numerical approach at 1st and 5th year. The horizontal and vertical error bars in (e) and (f) mean the differences between the numerical approach and the approach without considering wellbore lateral heat transfer. The injection flow rate in the reference case is 25 L s^{-1}.

number of supporting wells. With few supporting wells, the storage space for fluid is limited and unevenly distributed, whereas with more supporting wells, the storage space is large and more evenly distributed. In the first year, with a constant amount of injected heat, a great number of supporting wells results in more areas contacting the surroundings, reduced flow velocity and increased travel time within the wellbores. As a result, in the initial cycles, less heat is extracted from the produced fluid, and more heat remains stored in the reservoir, leading to great reservoir heat losses (Fig. 6 (c)). However, over long-term operation (e. g., 10+ cycles), the thermal plume is expected to become more evenly distributed, potentially improving system efficiency by reducing overall heat losses. Although the case with three supporting wells produces the largest volume of fluid in the first year (Fig. 6 (e)), the volume of the thermal fluid accumulation area predominantly influences the energy recovery efficiency (Fig. 6 (a)) and reservoir heat loss (Fig. 6 (c), which are negatively and positively correlated with the number of supporting wells, respectively. By the fifth year, cases with a high number of supporting wells (such as 3 or 4) achieve more uniform heating of the wellbore area. This results in reduced heat loss in the reservoir (Fig. 6 (c)), high heat production compared to cases with few supporting wells (Fig. 6 (a)) and a large volume of produced fluid (Fig. 6 (e)). In the first year, the linear relationship between the variations in energy recovery efficiency and wellbore lateral heat loss fraction with changes in number of supporting wells implies that number of supporting wells negatively impacts energy recovery efficiency and positively affects wellbore lateral heat loss fraction in a linear manner (Fig. 6 (d)). The case with 3 supporting wells demonstrates best performance in improving energy recovery efficiency to above 0.5 and diminishing wellbore lateral heat loss to less than 0.1 (Fig. 6 (d)). This suggests that optimizing the number of supporting well presents an opportunity to enhance the HT-ATES performance while simultaneously reducing drilling costs.

3.3. Effects of operational parameters

3.3.1. Injection flow rate

In this part, we consider seven different injection flow rates from the main well in the storage period or from all the supporting wells in the extraction period, ranging evenly from 6.25 to 25 L s^{-1}. The annual energy recovery efficiency and reservoir heat loss fraction under varying injection flow rates are illustrated in Fig. 7(a–d). The differences in the ranges and variations of energy recovery efficiency, extracted energy and wellbore lateral heat loss fraction between the numerical approach and the approach without considering wellbore lateral heat transfer, influenced by changes in injection flow rate, are summarized from the 1st to the 5th year in Fig. 7(e) and (f). As shown in Fig. 7 (a), the energy recovery efficiency increases with high injection flow rates, which also boosts the annual extracted energy (Fig. 7 (b)). In contrast, both the wellbore lateral heat loss fraction (Fig. 7 (c)) and the reservoir heat loss fraction (Fig. 7 (d)) decrease with increasing injection flow rates. The magnitudes of the error bars for energy recovery efficiency, extracted energy and wellbore lateral heat loss fraction between the numerical approach and the approach that excludes wellbore lateral heat transfer decrease with the rise of injection flow rate (Fig. 7(e) and (f)).

Without constraining the total injected energy and with a fixed injection fluid temperature, an increase in injection flow rate results in a great amount of heat being injected (E_{inj}) and extracted (E_{ext}) from the reservoir per unit time (Equations (7) and (8); Fig. 7 (b)). High injection flow rates also reduce the fluid's residence time in the wellbore, which decreases the period available for heat dissipation. This effect is more pronounced at high injection flow rates where temperature differences are greater, leading to reduced heat loss along the wellbore (Fig. 7 (c)). At low injection flow rates, the slow movement of fluid within the reservoir enhances thermal diffusion, which reduces the amount of heat that can be extracted. Conversely, high injection flow rates enable more efficient heat extraction before significant thermal diffusion occurs, thereby minimizing its impact (Fig. 7 (d)). Moreover, high injection flow

rates reduce the heat loss per unit of fluid, leading to higher system efficiency (Fig. 7(a)). For a specific fluid unit, the amount of heat lost during its circulation through the system directly affects the overall efficiency: the more heat lost, the lower the efficiency. When the fluid flows faster, it results in less heat loss per unit of fluid. Integrating this effect over all fluid units in the system, higher flow rates lead to lower overall heat losses and thus higher system efficiency. The cases with injection flow rates between 15.625 L s^{-1} and 25 L s^{-1} exhibit better performance in improving energy recovery efficiency to above 0.5 and diminishing wellbore lateral heat loss less than 0.1 (Fig. 7(e) and (f)). It should be noted that no upper bottom-hole pressure (BHP) limit was imposed in these simulations. In practical applications, constraints such as lithostatic pressure or maximum allowable wellbore pressure may limit feasible flow rates and wellbore diameters. Optimizing the injection flow rate is essential for improving the performance of an HT-ATES system. It requires balancing multiple factors, such as energy demand, pumping requirements and key performance indicators. By selecting the appropriate injection flow rate, the system's efficiency can be significantly enhanced, leading to reduced operational costs and a more effective overall system design.

3.3.2. Injection temperature at the main well

In this example, we examine seven different injection temperatures at the main well ranging from 90 °C to 210 °C to evaluate their effects on the system's performance. The injection temperature at supporting well in extraction period is fixed at 50 °C. As shown in Fig. 8 (a), both energy recovery efficiency and extracted energy increase with rising injection temperatures at the main well. Conversely, the wellbore lateral heat loss fraction (Fig. 8 (b)) and reservoir heat loss fraction (Fig. 8 (c)) decrease as the injection temperature at the main well increases. An increase in injection temperature at the main well amplifies the temperature difference between the injected fluid and the reservoir's in-situ temperature. According to Equations (7) and (8), this results in a great amount of heat being injected and extracted (Fig. 8 (b)). Additionally, as indicated by Equation (10), a high injection temperature at the main well causes a large temperature gradient between the wellbore and surrounding formation, thus leading to an increased heat transfer between these two regions, i.e., high net heat loss along the wellbore. Similarly, the rise in injection temperature increases the temperature difference between the injected fluid and the aquifer, resulting in higher net reservoir heat loss. However, both the wellbore lateral heat loss fraction and reservoir heat loss fraction decrease because the increase in injected energy is much more efficient than the increase in conductive heat loss through the wellbore and the reservoir. This results in a great fraction of high-temperature heat being extracted from the reservoir and reduces overall heat losses (including both wellbore and reservoir heat losses), thereby improving the energy recovery efficiency (Fig. 8 (a)). The differences in the ranges and variations of energy recovery efficiency, extracted energy and wellbore lateral heat loss fraction between the numerical approach and the approach without considering wellbore lateral heat transfer, influenced by changes in injection temperatures at the main well, are summarized from the 1st to the 5th year in Fig. 8(e) and (f). With the rise of injection temperatures at the main well, the magnitudes of the error bars for energy recovery efficiency, extracted energy and wellbore lateral heat loss fraction between the numerical approach and the approach that excludes wellbore lateral heat transfer decrease. Up until the fifth year, there are minor differences in energy recovery efficiency and wellbore lateral heat loss fraction due to the fully heated conditions in the aquifer. The impact of injection temperature on an HT-ATES system's performance is multifaceted, directly affecting heat storage efficiency, heat loss, energy consumption and overall economic benefits. Optimizing the injection temperature can maximize the economic benefits by balancing the efficiency of heat recovery with the costs associated with energy consumption and heat loss, leading to a more profitable operation.
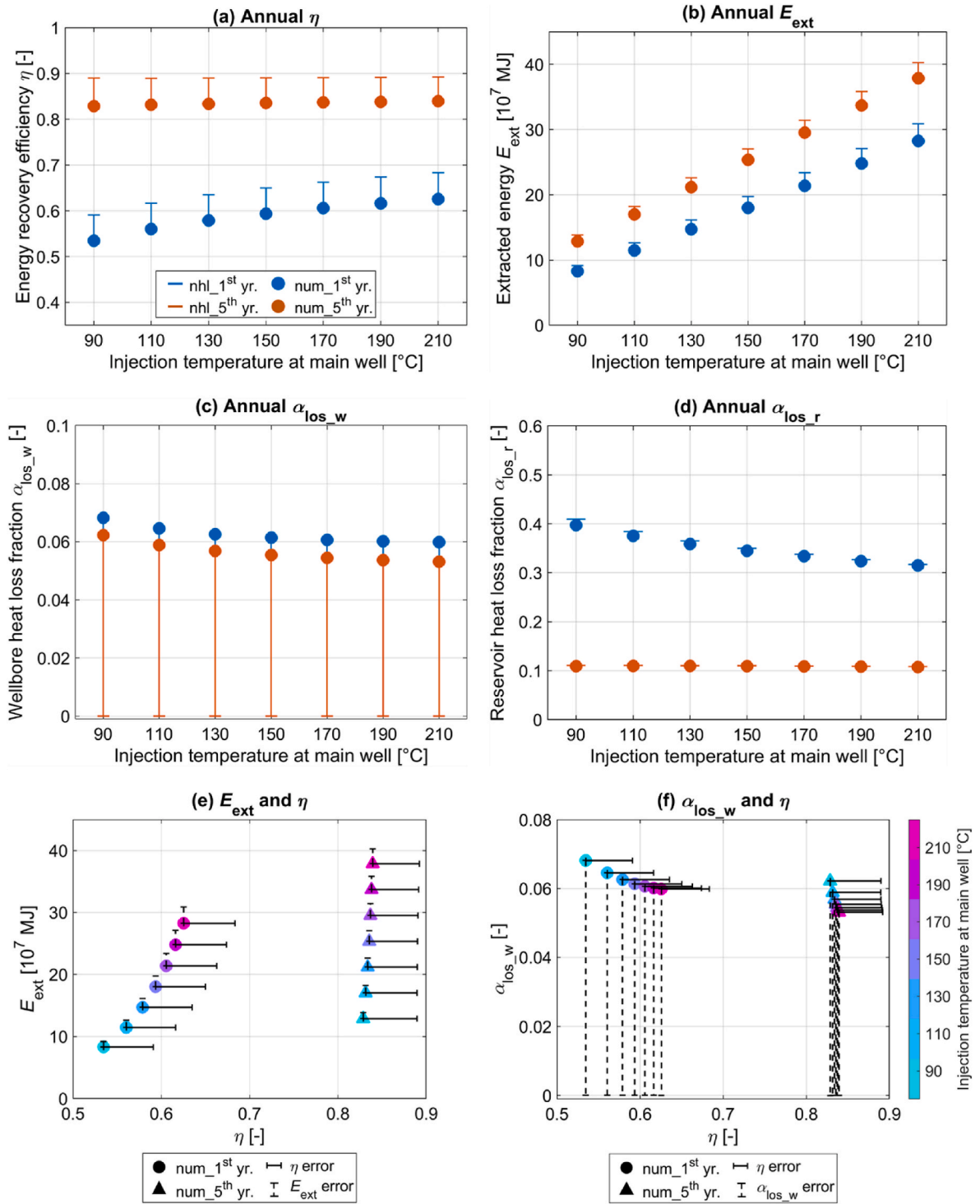
Fig. 8. The impact of injection temperature at the main well on the annual (a) energy recovery efficiency; (b) extracted energy; (c) wellbore lateral heat loss fraction; (d) reservoir heat loss fraction; (e) extracted energy versus energy recovery efficiency, and (f) wellbore lateral heat loss fraction versus energy recovery efficiency from the numerical approach at 1st and 5th year. The horizontal and vertical error bars in (e) and (f) mean the differences between the numerical approach and the approach without considering wellbore lateral heat transfer. The injection temperature at the main well in the reference case is 90 °C.

4. Conclusions

In this work, we investigated the impact of wellbore lateral heat transfer on the performance of HT-ATES systems. Our study focused on a specific HT-ATES project (the Swiss Bern project (Vidal et al., 2022)) using a five-spot system and numerically evaluated different ATES performance indicators including energy recovery efficiency, extracted energy, wellbore lateral heat loss fraction and reservoir heat loss fraction. We also examined how various wellbore configurations and operational parameters affect the HT-ATES performance, particularly due to the changes of the wellbore lateral heat loss. The key conclusions for this specific project can be listed as follows.

- Based on the reference case, the wellbore lateral heat loss can diminish the energy recovery efficiency of the HT-ATES system by around 7 %, which reflects the necessity of considering the wellbore in the ATES performance evaluation rather than ignoring the wellbore.

  o The analytical approach to calculate the wellbore heat loss gives rise to slightly lower values than the numerical one, thus leading to a higher energy recovery efficiency.

  o This study compares the two approaches to verify the reliability of analytical method. While numerical solutions are more realistic, they are computationally complex. Analytical methods, though less accurate, save computational time, especially in non-open-hole sections where advective heat transfer can be neglected. For open-hole sections, numerical methods are necessary due to fluid flow. The goal is not to favor one method but to highlight their differences and appropriate use cases.

- Using a small wellbore diameter can enhance the energy recovery efficiency of ATES, while large wellbore diameters lead to increased wellbore lateral and reservoir heat losses due to low fluid extraction volumes. The small diameter lowers the drilling costs but generates high wellbore pressure drops thus increasing the energy consumption for pumps.

- Wellbore casing materials with low thermal conductivity (e.g., fiberglass), improve the ATES system performance (energy recovery efficiency) by minimizing wellbore lateral heat loss to 3.3 %, which is approximately 51.4 % less than in the reference case.

- Regarding the number of supporting wells, energy recovery efficiency decreases with more wells in the first storage cycle due to the large space of reservoir heating. However, the case with three supporting wells demonstrates the best performance in the last cycle, mainly affected by the large extracted fluid volume from the warm reservoir condition.

- High flow rates enhance energy recovery efficiency and extracted energy while decreasing both wellbore and reservoir heat losses. This improvement results from the fast injection and production of fluid, which relatively reduces fluid residence time and thermal diffusion. While high flow rates can enhance convective heat transfer and reduce wellbore lateral heat losses, they may also lead to early thermal breakthrough at the production wells. This can shorten the duration of the heat storage phase, potentially resulting in extended idle periods where stored heat dissipates into the surrounding formation via conduction, ultimately reducing long-term energy recovery efficiency.

- High fluid injection temperatures at the main well can increase both wellbore and reservoir heat loss. However, the fractions of the wellbore and reservoir heat loss decrease due to the large amount of energy injected.

In conclusion, this study underscores the significance of wellbore lateral heat loss in the evaluation of the HT-ATES system performance. Our findings indicate that wellbore configurations and operational parameters should be carefully considered for designing an effective HT-ATES system. Although the studied parameters can give an impact on the energy recovery efficiency in a monotonous manner, other relevant factors such as material price, supply energy for hydraulic pump and drilling cost must be taken into account in order to find the optimal design solution of HT-ATES system. This study primarily investigates the initial phase of HT-ATES operations, covering the first five cycles. However, in real-world applications, HT-ATES systems are expected to operate for 30+ years, and steady-state conditions may only be reached after many cycles. Future studies should extend the simulation period to capture long-term thermal and hydrodynamic trends.

CRediT authorship contribution statement

Guoqiang Yan: Writing – original draft, Visualization, Validation, Software, Investigation, Data curation. **Pål Østebø Andersen:** Writing – review & editing. **Yangyang Qiao:** Writing – review & editing, Writing – original draft, Supervision, Investigation, Formal analysis, Conceptualization. **Dimitrios Georgios Hatzignatiou:** Writing – review & editing. **Bo Feng:** Writing – review & editing. **Thomas Kohl:** Writing – review & editing.

Declaration of competing interest

The authors declare the following financial interests/personal relationships which may be considered as potential competing interests: Guoqiang Yan reports financial support was provided by China Scholarship Council. If there are other authors, they declare that they have no known competing financial interests or personal relationships that could have appeared to influence the work reported in this paper.

Acknowledgments

Appendix I. Numerical algorithm of fully coupled wellbore-reservoir simulator

Taking the open-hole section as an example in Fig. A1 (a), the 1D wellbore intersects the center position of a column of formation grid blocks. The wellbore works as a line source, meaning that fluid and heat can flow out of or into the coupled reservoir grid block along the whole element lines (red

dots in Fig. A1 (a)). Simultaneously, the corresponding reservoir grids conservatively exchange the mass and energy with the wellbore elements. Space distributions of variables are based on the linear interpolation of their nodal values. The fluid properties in the coupling terms (Table 2) are evaluated based on the upstream method (fluid flow direction), which is only from either the wellbore or reservoir. The numerical algorithm for solving the coupled wellbore-reservoir model is illustrated in Fig. A1 (b).
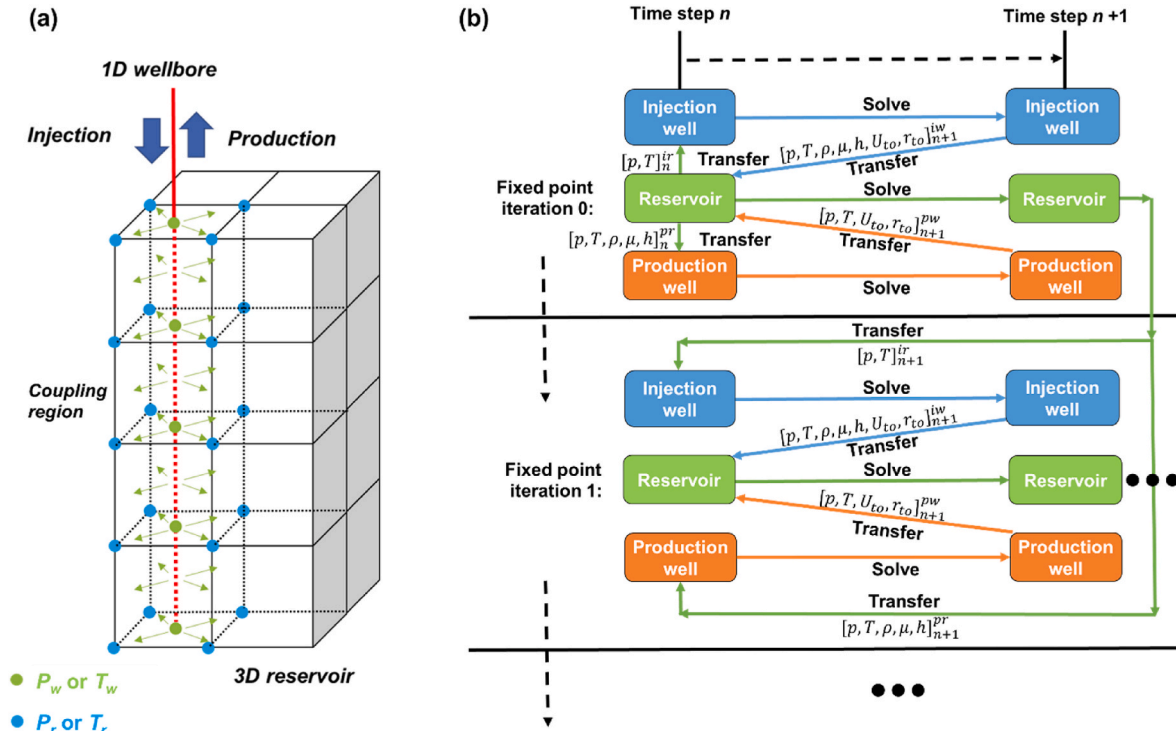

Fig. A1. Illustration of (a) the full coupling between the 1D wellbore simulator and the 3D reservoir simulator using the FEM; (b) numerical algorithm of the fully coupled simulator at each time interval (i.e., between time step n and time step $n+1$).

1) Wellbore modeling: At the first iteration, given the initial pressure, temperature and fluid properties (i.e., density, viscosity and enthalpy) from the reservoir's coupling grids, the wellbore simulator is employed to simulate the fluid flow and heat transfer processes, implicitly.
2) Reservoir modeling: Secondly, the corresponding results from the wellbore simulator's coupling grids are transferred into the reservoir simulator, as inputs. The reservoir modeling results are then fed back into the wellbore simulator for the next iteration.
3) Coupling iterations: There are two iterations for this coupled simulation. One is the inner iteration for solving each simulator (reservoir or wellbore), the convergence criteria should be satisfied with the Newton-Raphson method. The convergence criteria for the inner iteration were based on both nonlinear and linear relative and absolute tolerances, all set to 10^{-8} for variables, including pressure, temperature and flow rate. Another one is the outer iteration (i.e., coupling) between the wellbore and reservoir simulators by simply transferring coupling data between them. The outer iteration was implemented using MultiApp in MOOSE. Additionally, MOOSE's executioners provided fixed-point iteration algorithms to ensure tight coupling. For the outer iteration, the relative and absolute tolerances were set to 10^{-5} for coupling data, including pressure and temperature. Once the convergence criterion is met, we move to the next time step for new computations.

Appendix II Validation of numerical model for lateral heat transfer in the wellbore

To validate the borehole heat transport process in the wellbore-reservoir simulator, we conducted a benchmark simulation and compared the results with Ramey Jr (1962) analytical solution. The benchmark simulates a 30 m horizontal pipeline (see Table A1 for rock and fluid properties) in the subsurface, with circulation fluid flowing at $2 \bullet 10^{-4} \, \text{m}^3 \, \text{s}^{-1}$. The inlet fluid temperature is set at 20 °C, while the surrounding soil or rock begins at 55 °C.

Table A1
Rock and fluid properties of the reservoir and wellbore systems.

Regions	Properties	Symbols	Units	Values
Reservoir	porosity	ϕ	-	0
	permeability	k	m^2	0
	density	ρ_s	kg m^{-3}	2600
	specific heat capacity	$c_{p,s}$	$\text{J kg}^{-1} \text{K}^{-1}$	850
	thermal conductivity	λ_s	$\text{W m}^{-1} \text{K}^{-1}$	2.78
Wellbore	inner casing diameter	r_{ci}	m	0.25826

(continued on next page)

Table A1 (*continued*)

Regions	Properties	Symbols	Units	Values
	outer casing diameter	r_{co}	m	0.27
	cement/formation interface wellbore diameter	r_{cf}	m	0.28
	casing thermal conductivity	λ_{cas}	W m^{-1} K^{-1}	45
	cement thermal conductivity	λ_{cem}	W m^{-1} K^{-1}	1.1
Fluid	flow rate	Q_l	m^3 s^{-1}	$2 \bullet 10^{-4}$
	density	ρ_l	J kg^{-1} K^{-1}	1000
	thermal conductivity	λ_l	W m^{-1} K^{-1}	0.59
	dynamic viscosity	μ_l	Pa s	$1.14 \bullet 10^{-3}$
	specific heat capacity	$c_{p,l}$	J kg^{-1} K^{-1}	4190
	roughness	f	m	10^{-4}

As the fluid circulates, its lower temperature gradually cools the surrounding formation. The simulated evolution of the wellbore outlet circulation fluid temperature is compared with Ramey's analytical solution (see Fig. A2). The main discrepancy occurs at the start of the simulation due to the influence of the wellbore's initial temperature and cement heat capacity in the numerical model, which are not accounted for in Ramey's solution. In the numerical model, it takes nearly 0.1 days for the initial fluid to drain, resulting in a slight delay and causing the numerical results to shift forward (see red line in Fig. A2). Additionally, the inclusion of cement heat conduction leads to a slower temperature decline in the numerical model compared to the analytical solution. Despite these initial differences, the two results converge as the simulation progresses, and heat transfer becomes dominated by formation heat conduction after about one day (Fig. A2).
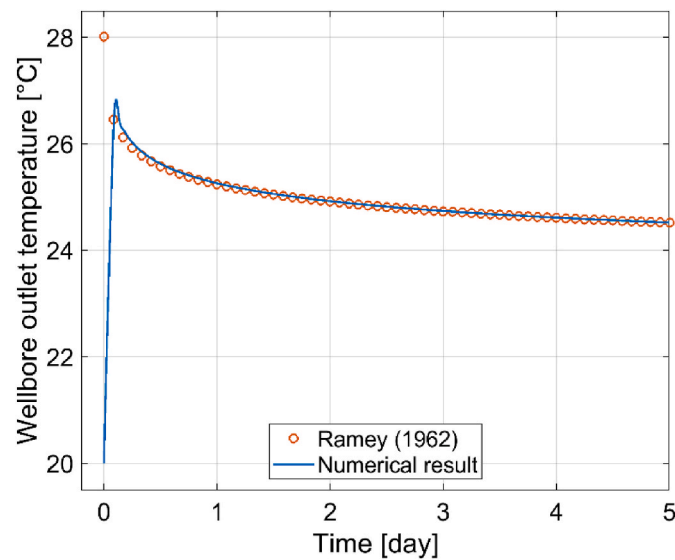

Fig. A2. Simulated wellbore outlet fluid temperature during the first 5 days, compared with the analytical solution of Ramey Jr (1962).

Appendix III. Supplementary contents

During the storage phase, the fluid production from the supporting wells with different diameters can be divided into three phases.

1) initial period with less fluid production of larger diameter cases than smaller diameter cases (Fig. A3 (a)): Since fluid production operates based on the pressure differential between the wellbore and the surrounding aquifer, the initial pressure build-up around the main well is less pronounced in the larger wellbore diameter case. The smaller pressure differential between the supporting wells and the aquifer results in reduced fluid production from the supporting wells during this initial period.
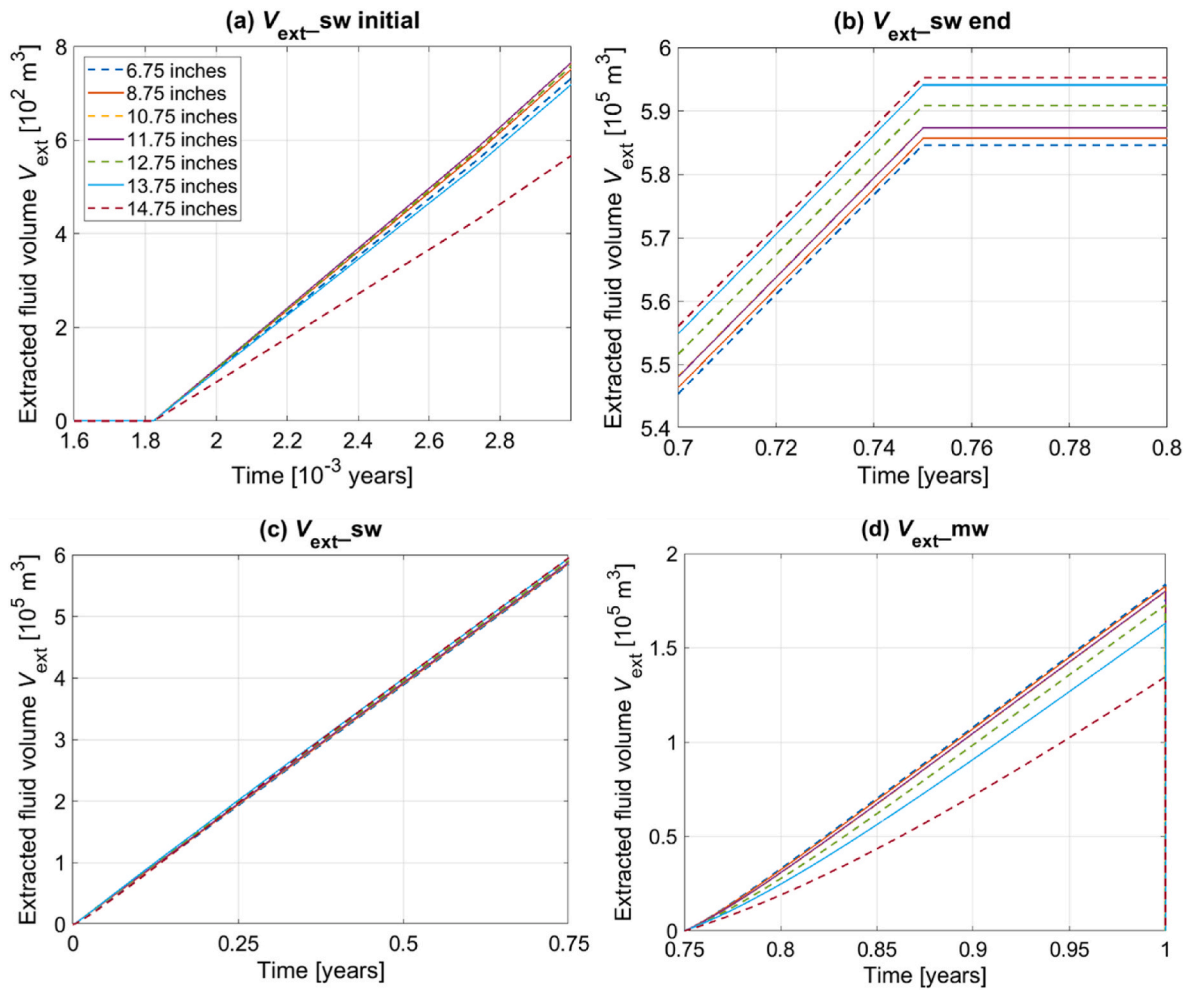
Fig. A3. Effects of wellbore diameter on numerical solutions of annual extracted fluid volume from (c) supporting wells at the initial time (a) and at the end time (b) within 1st storage phase; (d) main well within the 1st extraction phase.

2) later period with increased fluid production of larger diameter cases (Fig. A3 (b)): as the main well continues to inject fluid, the larger diameter allows for more efficient fluid movement in the reservoir. While the reservoir pressure increase in the larger wellbore diameter case is slower and less than in the smaller diameter case, the improved fluid mobility over time leads to a larger driving force for fluid flow toward the supporting wells. The higher *WI* values of the larger wellbore diameter wells further enhance this flow, resulting in increased fluid production during this later phase.

3) final period with the same fluid production (Fig. A3 (c)): Eventually, fluid production rates from the supporting wells stabilize and become similar regardless of wellbore diameter. At this point, the system has reached a balance where both large and small-diameter wells produce at comparable rates.

Data availability

Data will be made available on request.

References

Anwar, I., Chojnicki, K., Bettin, G., Taha, M.R., Stormont, J.C., 2019. Characterization of wellbore casing corrosion product as a permeable porous medium. J. Petrol. Sci. Eng. 180, 982–993.

Barbier, E., 2002. Geothermal energy technology and current status: an overview. Renew. Sustain. Energy Rev. 6 (1–2), 3–65.

Beernink, S., Hartog, N., Vardon, P.J., Bloemendal, M., 2024. Heat losses in ATES systems: the impact of processes, storage geometry and temperature. Geothermics 117, 102889.

Bloemendal, M., Hartog, N., 2018. Analysis of the impact of storage conditions on the thermal recovery efficiency of low-temperature ATES systems. Geothermics 71, 306–319.

Brown, C.S., Falcone, G., 2024. Investigating heat transmission in a wellbore for Low-Temperature, Open-Loop geothermal systems. Therm. Sci. Eng. Prog. 48, 102352.

Cheng, W., Huang, Y., Lu, D., Yin, H., 2011. A novel analytical transient heat-conduction time function for heat transfer in steam injection wells considering the wellbore heat capacity. Energy 36 (7), 4080–4088.

Dickinson, J.S., Buik, N., Matthews, M.C., Snijders, A., 2009. Aquifer thermal energy storage: theoretical and operational analysis. Geotechnique 59 (3), 249–260.

Dincer, I., 2002. Thermal energy storage systems as a key technology in energy conservation. Int. J. Energy Res. 26 (7), 567–588.

Doughty, C., Hellström, G., Tsang, C.F., Claesson, J., 1982. A dimensionless parameter approach to the thermal behavior of an aquifer thermal energy storage system. Water Resour. Res. 18 (3), 571–587.

Duijff, R., Bloemendal, M., Bakker, M., 2023. Interaction effects between aquifer thermal energy storage systems. Groundwater 61 (2), 173–182.

EIA, 2009. Residential energy consumption survey. US Energy Inf. Adm.

EU, 2010. In: Union, O.J.o.t.E. (Ed.), Directive on the Energy Performance of Buildings 153.

Ezekiel, J., Ebigbo, A., Adams, B.M., Saar, M.O., 2020. Combining natural gas recovery and CO2-based geothermal energy extraction for electric power generation. Appl. Energy 269, 115012.

Geuzaine, C., Remacle, J.F., 2009. Gmsh: a 3-D finite element mesh generator with built-in pre-and post-processing facilities. Int. J. Numer. Methods Eng. 79 (11), 1309–1331.

Guo, C., Zhang, K., Pan, L., Cai, Z., Li, C., Li, Y., 2017. Numerical investigation of a joint approach to thermal energy storage and compressed air energy storage in aquifers. Appl. Energy 203, 948–958.

Hasan, A.R., Kabir, C.S., 1991. Heat transfer during two-phase flow in wellbores: part I—formation temperature. In: SPE Annual Technical Conference and Exhibition? SPE, pp. SPE-22866.

Henry, A., Prasher, R., Majumdar, A., 2020. Five thermal energy grand challenges for decarbonization. Nat. Energy 5 (9), 635–637.

Horne, R.N., Shinohara, K., 1979. Wellbore heat loss in production and injection wells. J. Petrol. Technol. 31 (1), 116–118.

Huang, Y., Pang, Z., Kong, Y., Watanabe, N., 2021. Assessment of the high-temperature aquifer thermal energy storage (HT-ATES) potential in naturally fractured geothermal reservoirs with a stochastic discrete fracture network model. J. Hydrol. 603, 127188.

IEA, 2019. Renewables 2019 - analysis and forecast to 2024. Retrieved from. https://iea.blob.core.windows.net/assets/a846e5cf-ca7d-4a1f-a81b-ba1499f2cc07/Renewables_2019.pdf.

Jäger-Waldau, A., 2007. Photovoltaics and renewable energies in Europe. Renew. Sustain. Energy Rev. 11 (7), 1414–1437.

Kallesøe, A.J., Vangkilde-Pedersen, T., Guglielmetti, L., 2020. HEATSTORE–underground thermal energy storage (UTES)-state of the art, example cases and lessons learned. In: Proceedings World Geothermal Congress, p. 1.

Kangas, M.T., Lund, P.D., 1994. Modeling and simulation of aquifer storage energy systems. Sol. Energy 53 (3), 237–247.

Kim, J., Lee, Y., Yoon, W.S., Jeon, J.S., Koo, M.H., Keehm, Y., 2010. Numerical modeling of aquifer thermal energy storage system. Energy 35 (12), 4955–4965.

Korzani, M.G., Nitschke, F., Held, S., Kohl, T., 2019. The development of a fully coupled wellbore-reservoir simulator for geothermal application. In: Geothermal: Green Energy for the Long Run-Geothermal Resources Council 2019 Annual Meeting, GRC 2019. Geothermal Resources Council, pp. 927–936.

Lee, K.S., Lee, K.S., 2013. Underground Thermal Energy Storage. Springer, London, pp. 15–26.

Li, Y., Yu, H., Luo, X., Liu, Y., Zhang, G., Tang, D., Liu, Y., 2023a. Full cycle modeling of inter-seasonal compressed air energy storage in aquifers. Energy 263, 125987.

Li, Y., Yu, H., Xiao, Y., Liu, Y., Luo, X., Tang, D., et al., 2023b. Numerical verification on the feasibility of compressed carbon dioxide energy storage in two aquifers. Renew. Energy 207, 743–764.

Li, Y., Yu, H., Tang, D., Zhang, G., Liu, Y., 2024. Study on the applicability of compressed carbon dioxide energy storage in aquifers under different daily and weekly cycles. Renew. Energy 222, 119987.

Livescu, S., Durlofsky, L.J., Aziz, K., Ginestra, J.C., 2008. Application of a new fully-coupled thermal multiphase wellbore flow model. In: SPE Improved Oil Recovery Conference, pp. SPE–113215. SPE.

Livescu, S., Durlofsky, L.J., Aziz, K., Ginestra, J.C., 2010. A fully-coupled thermal multiphase wellbore flow model for use in reservoir simulation. J. Petrol. Sci. Eng. 71 (3–4), 138–146.

Mohammed, A.I., Oyeneyin, B., Atchison, B., Njuguna, J., 2019. Casing structural integrity and failure modes in a range of well types-a review. J. Nat. Gas Sci. Eng. 68, 102898.

Muhammed, G., Tekbiyik-Ersoy, N., 2020. Development of renewable energy in China, USA, and Brazil: a comparative study on renewable energy policies. Sustainability 12 (21), 9136.

Oldenburg, C.M., Pan, L., 2013. Porous media compressed-air energy storage (PM-CAES): theory and simulation of the coupled wellbore–reservoir system. Transport Porous Media 97, 201–221.

Paksoy, H.O., Gürbüz, Z., Turgut, B., Dikici, D., Evliya, H., 2004. Aquifer thermal storage (ATES) for air-conditioning of a supermarket in Turkey. Renew. Energy 29 (12), 1991–1996.

Pan, L., Oldenburg, C.M., 2014. T2Well—an integrated wellbore–reservoir simulator. Comput. Geosci. 65, 46–55.

Peaceman, D.W., 1983. Interpretation of well-block pressures in numerical reservoir simulation with nonsquare grid blocks and anisotropic permeability. Soc. Petrol. Eng. J. 23 (3), 531–543.

Permann, C.J., Gaston, D.R., Andrš, D., Carlsen, R.W., Kong, F., Lindsay, A.D., et al., 2020. MOOSE: enabling massively parallel multiphysics simulation. SoftwareX 11, 100430.

Pribnow, D.F., Sass, J.H., 1995. Determination of thermal conductivity for deep boreholes. J. Geophys. Res. Solid Earth 100 (B6), 9981–9994.

Ramey Jr, H.J., 1962. Wellbore heat transmission. J. Petrol. Technol. 14 (4), 427–435.

Satter, A., 1965. Heat losses during flow of steam down a wellbore. J. Petrol. Technol. 17 (7), 845–851.

Schüppler, S., Fleuchaus, P., Blum, P., 2019. Techno-economic and environmental analysis of an Aquifer Thermal Energy Storage (ATES) in Germany. Geoth. Energy 7, 1–24.

Sharmin, T., Khan, N.R., Akram, M.S., Ehsan, M.M., 2023. A state-of-the-art review on geothermal energy extraction, utilization, and improvement strategies: conventional, hybridized, and enhanced geothermal systems. Int. J. Thermofluids 18, 100323.

Sheldon, H.A., Wilkins, A., Green, C.P., 2021. Recovery efficiency in high-temperature aquifer thermal energy storage systems. Geothermics 96, 102173.

Shi, D., Cheng, S., Wang, Q., Liu, D., Yin, Fu, Xu, X., Guo, X., Weng, Z., 2024. Comparative analysis and application of mass and heat transfer simulation in fractured reservoirs based on two fracture models. Processes 12 (11), 1–25.

Sommer, W., Valstar, J., van Gaans, P., Grotenhuis, T., Rijnaarts, H., 2013. The impact of aquifer heterogeneity on the performance of aquifer thermal energy storage. Water Resour. Res. 49 (12), 8128–8138.

Stemmle, R., Blum, P., Schüppler, S., Fleuchaus, P., Limoges, M., Bayer, P., Menberg, K., 2021. Environmental impacts of aquifer thermal energy storage (ATES). Renew. Sustain. Energy Rev. 151, 111560.

Tsang, C.F., 1978. Aquifer thermal energy storage. Institute of Gas Technology Symposium on Advanced Technologies for Storing Energy, Chicago, ILL.

United Nations, 2015. Framework convention on climate change. Adoption of the Paris agreement.

Ürge-Vorsatz, D., Cabeza, L.F., Serrano, S., Barreneche, C., Petrichenko, K., 2015. Heating and cooling energy trends and drivers in buildings. Renew. Sustain. Energy Rev. 41, 85–98.

Usman, O., Akadiri, S.S., Adeshola, I., 2020. Role of renewable energy and globalization on ecological footprint in the USA: implications for environmental sustainability. Environ. Sci. Pollut. Control Ser. 27 (24), 30681–30693.

van der Roest, E., Beernink, S., Hartog, N., van der Hoek, J.P., Bloemendal, M., 2021. Towards sustainable heat supply with decentralized multi-energy systems by integration of subsurface seasonal heat storage. Energies 14 (23), 7958.

van Lopik, J.H., Hartog, N., Schotting, R.J., 2022. Using multiple partially-penetrating wells (MPPWs) to improve the performance of high-temperature ATES systems: well operation, storage conditions and aquifer heterogeneity. Geothermics 105, 102537.

Vidal, R., Olivella, S., Saaltink, M.W., Diaz-Maurin, F., 2022. Heat storage efficiency, ground surface uplift and thermo-hydro-mechanical phenomena for high-temperature aquifer thermal energy storage. Geoth. Energy 10 (1), 23.

Wiktorski, E., Cobbah, C., Sui, D., Khalifeh, M., 2019. Experimental study of temperature effects on wellbore material properties to enhance temperature profile modeling for production wells. J. Petrol. Sci. Eng. 176, 689–701.

Wilkins, A., Green, C.P., Ennis-King, J., 2021. An open-source multiphysics simulation code for coupled problems in porous media. Comput. Geosci. 154, 104820.

Willhite, G.P., 1967. Over-all heat transfer coefficients in steam and hot water injection wells. J. Petrol. Technol. 19 (5), 607–615.

Wu, Y.S., Pruess, K., 1990. An analytical solution for wellbore heat transmission in layered formations. SPE Reserv. Eng. 5 (4), 531–538.

Xiong, W., Bahonar, M., Chen, Z., 2016. Development of a thermal wellbore simulator with focus on improving heat-loss calculations for steam-assisted-gravity-drainage steam injection. SPE Reservoir Eval. Eng. 19 (2), 305–315.

You, J., Rahnema, H., McMillan, M.D., 2016. Numerical modeling of unsteady-state wellbore heat transmission. J. Nat. Gas Sci. Eng. 34, 1062–1076.

Zhang, Y., Pan, L., Pruess, K., Finsterle, S., 2011. A time-convolution approach for modeling heat exchange between a wellbore and surrounding formation. Geothermics 40 (4), 261–266.